

Contents lists available at ScienceDirect

Petroleum Science





Original Paper

Multidisciplinary insights into the origin of natural gas from hydrocarbon generation and charging history of Permian dolomite reservoir in Sichuan Basin



Yan-Xian Zhu ^{a, b}, Zhi-Liang He ^{a, c, *}, Xiao-Wen Guo ^a, Long Li ^b, Kamaldeen O.L. Omosanya ^d, Jian Gao ^{e, f}, Ze Tao ^a, Xue-Song Lu ^g

- a Key Laboratory of Tectonics and Petroleum Resources, Ministry of Education, China University of Geosciences, Wuhan, 430074, Hubei, China
- ^b Department of Earth and Atmospheric Science, University of Alberta, Edmonton, T6G 2R3, Alberta, Canada
- ^c China Petroleum and Chemical Corporation, Beijing, 100027, China
- ^d Department of Geology and Geophysics, Oasisgeokonsult, 7052, Trondheim, Norway
- ^e SINOPEC Petroleum Exploration and Production Research Institute, Beijing, 102206, China
- f SINOPEC Key Laboratory of Geology and Resources in Deep Strata, Beijing, 102206, China
- g Research Institute of Petroleum Exploration and Development, PetroChina, Beijing, 100083, China

ARTICLE INFO

Article history: Received 8 June 2024 Received in revised form 30 October 2024 Accepted 11 February 2025 Available online 14 February 2025

Edited by Jie Hao and Meng-Jiao Zhou

Keywords: U-Pb dating Hydrocarbon generation and charging history Origin of natural gas Deep and ultra-deep carbonate reservoirs Sichuan Basin

ABSTRACT

Understanding the origin of natural gas in deep and ultra-deep reservoirs with multiple potential source rocks remains challenging due to the complex thermal evolution of hydrocarbons at high temperatures and multi-stage accumulation processes. This study investigates the origin of natural gas in deep hydrothermal dolomite reservoirs of the Maokou Formation, eastern Sichuan Basin, using hydrocarbon inclusion analysis, radiometric U-Pb dating of calcite cements, maturity modeling of potential source rocks, and constraints on reactivation periods of the nearby No. 15 Fault System. Results indicate an oil charging event at approximately 246.9 Ma, followed by two episodes of gas charging at 222.4 Ma and 175.2 Ma. Furthermore, the oil and gas charging events occurred synchronously with activities of the No. 15 Fault System, suggesting that its reactivation induced episodic hydrocarbon migration. Maturity modeling indicates that during the oil charging period, source rocks in the Qiongzhusi, Wufeng-Longmaxi, and first member of the Maokou formations reached the stages of dry gas generation, significant oil generation, and the threshold of oil generation, respectively. During the subsequent twoepisode gas charging periods, the Qiongzhusi and Wufeng-Longmaxi formations progressed to dry and wet gas generation stages, respectively, while the first member of the Maokou Formation attained the oil generation stage. The hydrocarbon charging time and maturity history of potential source rocks indicate that: 1) oil in hydrothermal dolomite reservoirs predominantly originated from the Wufeng-Longmaxi Formation at approximately 246.9 Ma; 2) during the subsequent gas charging episodes, the Wufeng-Longmaxi Formation could contribute wet gas, while the Qiongzhusi Formation likely supplied cracking gas from kerogen and residual liquid hydrocarbon; 3) all oil in the hydrothermal dolomite reservoirs underwent thermal cracking to gas at approximately 110 Ma. This study indicates that gas pools in (ultra-)deep carbonate reservoirs of the Sichuan Basin have mixed genetic origins, with contributions from multiple sources. The multidisciplinary approach, combining direct dating of hydrocarbon charge events and simulation of hydrocarbon generation, proves robust and effective in identifying the origin of natural gas in (ultra-)deep reservoirs.

© 2025 The Authors. Publishing services by Elsevier B.V. on behalf of KeAi Communications Co. Ltd. This is an open access article under the CC BY-NC-ND license (http://creativecommons.org/licenses/by-nc-nd/

4.0/).

1. Introduction

Understanding the genesis of natural gas is vital for unraveling the petroleum system and forecasting resource distribution (Huang

E-mail address: hezhiliang@cug.edu.cn (Z.-L. He).

Corresponding author.

et al., 2015; Li et al., 2022). The gas pools in the deep (>4500 m) and ultra-deep (>6000 m) reservoirs with multiple source intervals have been documented in various basins worldwide, including the Gulf of Mexico, USA (Loucks and Dutton, 2019); Adriatic Foreland Basin, Italy (Cazzini et al., 2015); Ghaba Salt Basin, Oman (Millson et al., 2008); and the Sichuan, Tarim, and Junggar basins, China (He et al., 2023). Gas and paleo-oil pools in deep and ultra-deep reservoirs have typically experienced high temperatures due to great burial depths. Understanding the natural gas origin in (ultra-) deep reservoirs with multiple potential source rocks remains challenging due to the complex thermal evolution of hydrocarbons and multi-stage accumulation processes (Liu et al., 2019; Zhang et al., 2021; Kotarba et al., 2022; He et al., 2023). Previous studies have attempted to determine the source and origin of natural gas in these reservoirs, predominantly using two approaches: 1) compositional analysis of the gas, including its component contents and corresponding carbon isotopes (Zou et al., 2014; Faramawy et al., 2016); 2) analysis of over-mature pyrobitumen, comprising its biomarker, carbon isotopes and rare earth elements (Jin et al., 2014; Chen et al., 2018). However, component analysis proves ineffective in tracing the source of gas pools with mixed contributions from kerogen-cracking and oil-cracking gases (Liu et al., 2019). The carbon isotopes of methane and ethane are primarily controlled by their thermal evolution, which can cause an isotopic reversal between these compounds at high temperatures (Liu et al., 2019). Few effective biomarkers can be extracted from over-mature pyrobitumen (Peters et al., 2005) due to the rapid degradation of biomarkers in the free pyrobitumen (Zhang et al., 2021). Carbon isotopes of pyrobitumen are occasionally unreliable due to their non-linear evolution during organic matter pyrolysis (Volkman et al., 1994; Kotarba et al., 2022) and alteration by thermochemical sulfate reduction (TSR) and oxidation reactions (Cai et al., 2017; Liang et al., 2020). It is unconvincing to trace the source of pyrobitumen by the similarity of rare earth elements between pyrobitumen and shales, owing to the different distributions of rare earth elements in major components (sulfide, silicate and organic) within shales (Abanda and Hannigan, 2006) and unclear partitioning of rare earth elements during the thermal evolution of organic (Bhattacharya et al., 2024).

The Sichuan Basin in southwest China has a complex geological history marked by several tectonic events, which have driven the evolution of the basin from a marine carbonate platform during the Ediacaran to Late Triassic period, a foreland basin during the Late Triassic to Late Cretaceous Indosinian-Yanshanian orogenies, and ultimate uplift and tectonic deformation from the Late Cretaceous to the Quaternary (Liu et al., 2021; He et al., 2022). The Tailai Gas Field, located within the Bashansi syncline of the Eastern Sichuan Basin (ESB), features large-scale hydrothermal dolomite reservoirs (HDR) in the third member of the Maokou Formation with the burial depth of approximately 5000 m (Yang et al., 2022). Within the Bashansi syncline, the No. 15 Fault System mainly comprising basement faults transects multiple potential source rocks, including the Qiongzhusi Formation, Wufeng-Longmaxi Formation, and the first member of the Maokou Formation acting as the primary conduit for vertical hydrocarbon migration. Previous studies investigated the origin and source of gas pools within the Permian Maokou Formation by component contents with their carbon isotopes of gas and biomarker composition of pyrobitumen in the study area (Xie et al., 2020; Li et al., 2021; Huang et al., 2023). However, the origin and source of natural gas in the HDR in the Maokou Formation are controversial in the Tailai Gas Field. Yang et al. (2022) identified multi-stage dolomite, calcite, and quartz cements within the third member of the Maokou Formation of the Tailai Gas Field. These cements hold promise for revealing the timing of hydrocarbon charge events. In-situ laser-ablation

radiometric (U-Pb) dating of carbonate cements is an advanced technique (Roberts et al., 2020, 2021) to determine the time of hydrocarbon charge in the sedimentary basins (Cong et al., 2021; Ni et al., 2024a). Micro-Laser Raman spectroscopy (LRM) is a microanalytical technique than enables to analyze the composition of fluid inclusions trapped within these cements (Burke, 2001; Zhang et al., 2016). Here, we employed a multidisciplinary approach that integrates geochemical, petrological, and geophysical techniques to better understand the source of natural gas in the HDR in the Maokou Formation in the Tailai Gas Field. In this study, we aim to constrain: (a) the hydrocarbon generation history by simulating the burial and thermal evolution of source rocks within the Tailai area of the ESB, (b) fault reactivation periods using 3D seismic data from the Tailai Gas Field to identify the reactivation and development periods of the No. 15 Fault System, (c) hydrocarbon charging time through a comprehensive analysis of minerals with the development of hydrocarbon inclusions, and (d) the origin of the natural gas charging into the carbonate reservoirs in the third member of the Maokou Formation based on the hydrocarbon generation and charging history.

This study's findings have implications beyond the Sichuan Basin, offering insights for deep hydrocarbon reservoir exploration worldwide. The multidisciplinary approach integrating hydrocarbon generation modeling, fault reactivation analysis, and direct dating of hydrocarbon charge events provides a robust framework for comprehensive assessment of gas sources in (ultra-)deep reservoirs within complex geological settings.

2. Geological setting

The Sichuan Basin, located in the western region of the Yangtze Block, covers an area of 18×10^4 km² and has a rhombic shape (Fig. 1). The basin characterized by a western depression, a central paleo-high, an eastern high steep fold-and-thrust belt, and a southern fold-and-thrust belt (Fig. 1). At a local scale, the Tailai Gas Field situated in the Bashansi syncline in the ESB, adjacent to the No. 15 Fault System (Zhang et al., 2020) (Fig. 1(a)). The ESB is bounded by the Huayingshan and Qiyueshan faults (Fig. 1(a)), and characterized by a thin-skinned Jura-type fold belt in its structural style (Li et al., 2015a; Gu et al., 2021) (Fig. 1(c)).

Analysis of seismic and borehole data reveals that the ESB was historically filled with marine sediments ranging from the Sinian to the Middle Triassic, alongside terrestrial deposits since the Late Triassic (Fig. 2). Recent studies have confirmed that source intervals include the Lower Cambrian Qiongzhusi Formation, the Wufeng-Longmaxi Formation and Middle Permian source rocks - the first member of the Maokou Formation in the ESB (Guo et al., 2020; Li et al., 2021). The Tailai Gas Field comprises HDR with a production rate of $15.32 \times 10^4 \, \mathrm{m}^3/\mathrm{d}$ (Zhang et al., 2020). The thickness of its dolomite reservoir - part of the third member of the Maokou Formation - varies from 10.7 m to 23.1 m (Pan et al., 2020). The Longtan Formation shale serves as the seal rock for the carbonate reservoirs in the third member of the Maokou Formation.

The multistage structural deformation observed in the ESB was intricately linked to the broader tectonic evolution of the South China continent. The amalgamation of the Yangtze block and the Cathaysian block formed the South China continent during the Jinning orogeny before 820 Ma (He et al., 2011; Zhang et al., 2013). In the early Cryogenian, the Sichuan basin developed a few basement faults with the strike of NW-SE and NE-SW in the Xingkai taphrogenesis (Gu and Wang, 2014). During the Early Cambrian, the Tongwan orogeny resulted in uplift of the Yangtze Block and erosion of the Dengying Formation in the Sichuan Basin (Li et al., 2015b). Subsequently, the Caledonian orogeny caused the uplift and exhumation of the Sichuan Basin during the Silurian (Charvet,

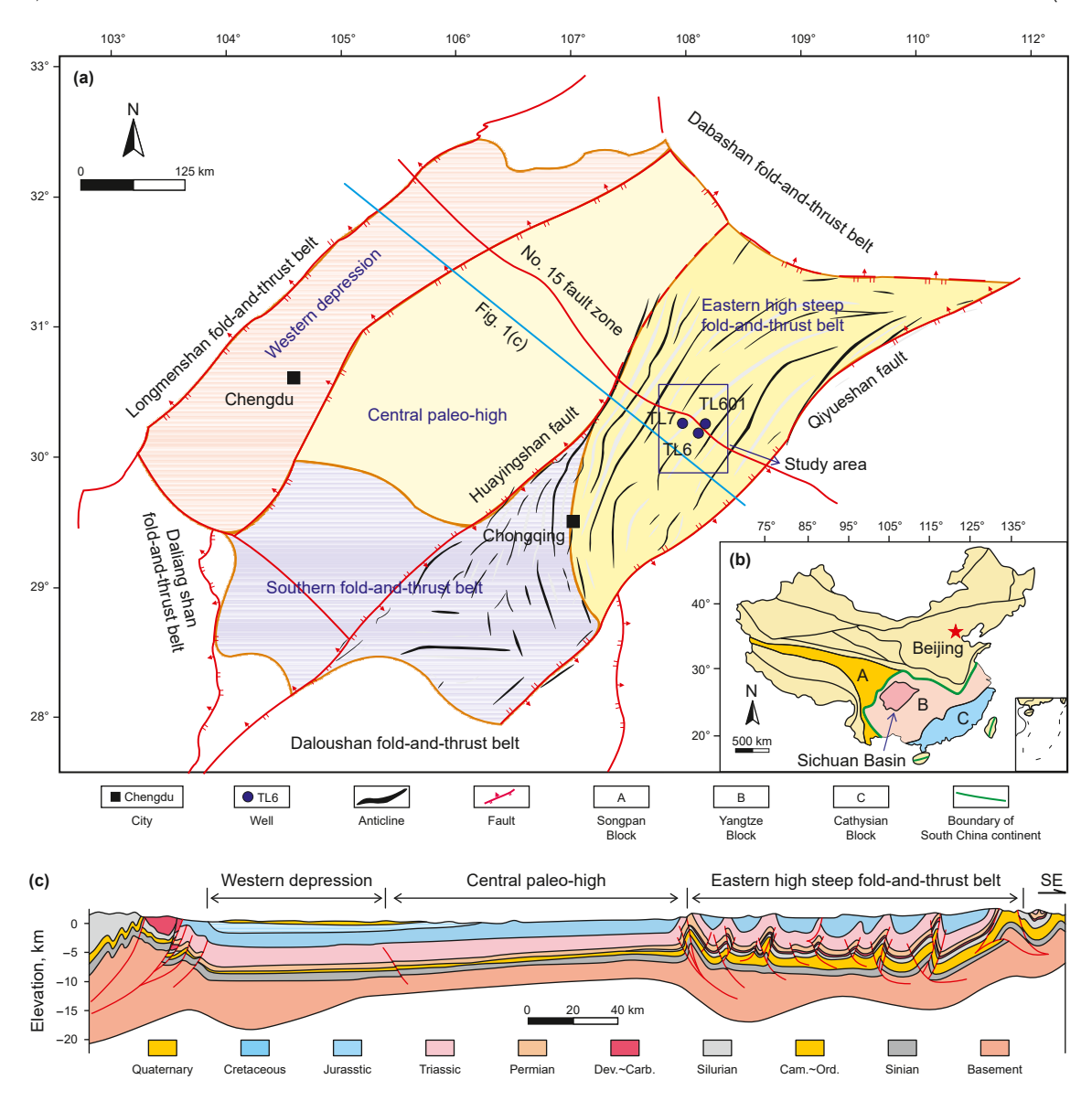


Fig. 1. (a) A regional tectonic map showing the distribution of faults in the Sichuan Basin (modified from He et al. (2011) and Zhang et al. (2020)) and the location of the study area in the Eastern Sichuan Basin. (b) A simplified tectonic map of China showing the location of the Sichuan Basin within the Upper Yangtze Block. (c) A simplified northwest to southeast geological cross-section across the Sichuan Basin shows its complex structural characteristics. Please note that the location of Fig. 1(c) is indicated by the cyan transect line in Fig. 1(a). Fig. 1(c) has been adapted from Liu et al. (2018b).

2013). The Hercynian orogeny further uplifted the Yangtze block from the Late Carboniferous to the Early Permian, triggering another uplift and exhumation in the Sichuan Basin (Horizon H2 in Fig. 2; Liu et al., 2021).

During the Permian Dongwu movement, the rise of the Emeishan mantle plume caused significant crustal uplift and erosion in the Yangtze Plate and Sichuan Basin (Jiang et al., 2018). The formation of the Emeishan Large Igneous Province during the Emei magmatism induced anomalous thermal events in the Sichuan Basin (Liang et al., 2013). During the Indosinian orogeny, the South China continent collided with the Indochina block from the Latest Permian to Middle Triassic, and further with the Songpan block in the Late Triassic (Harrowfield and Wilson, 2005; Liu et al., 2018a). The ESB was deformed at this time, which caused the formation of Luzhou High and an angular unconformity at the Top of the Leikoupo Formation — T₂I (Horizon H5 in Fig. 2).

The Yanshanian orogeny involved the subduction of the Paleo-Pacific crust under the South China continent (Li et al., 2012),

leading to further uplift and deformation of the Sichuan Basin under continuous NW-SE compressive stress. The thin-skinned Jura-type fold belt in the ESB was initially formed from the Early Jurassic to the earliest Cretaceous and underwent subsequent deformation in a late Cretaceous stage (Shi et al., 2016; Zheng et al., 2019; Li et al., 2024). Additionally, during the Himalayan orogeny spanning from the end of the Cretaceous to the Holocene, the South China continent experienced uplift and deformation due to the extrusion of the Songpan Block. This period of tectonic uplift, erosion, and extensive folding significantly influenced the present structural framework of the Sichuan Basin (Li et al., 2019).

3. Samples and methods

A total of 11 HDR core samples were obtained from the Middle Permian Maokou Formation in three wells (TL6, TL7 and TL601) of the Tailai Gas Field, ESB (Table 1). The 11 carbonate samples contain 1 sample with fracture- and vug-filling cements from Well TL6, 6

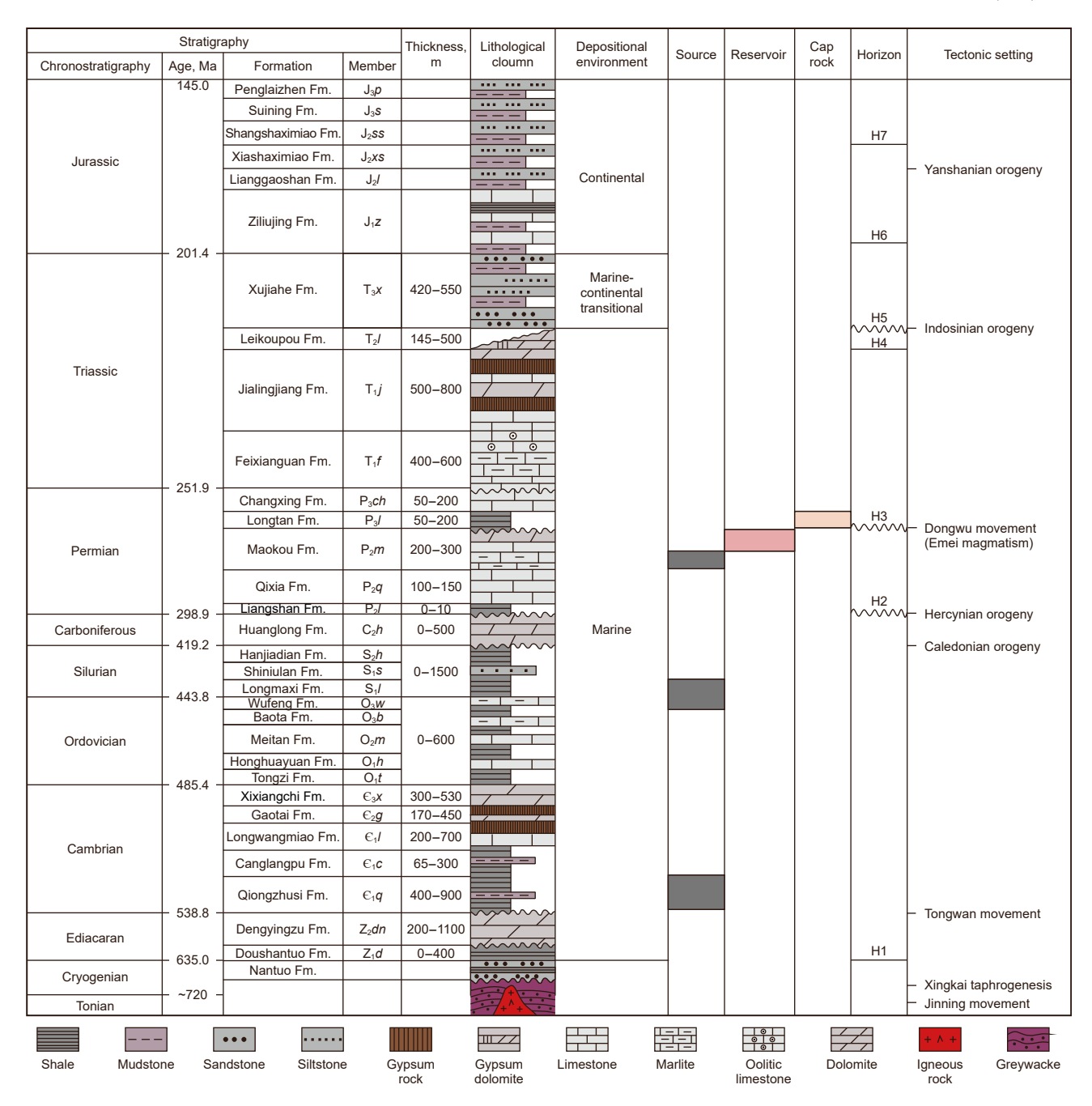


Fig. 2. Generalized Neoproterozoic to Jurassic stratigraphy of the Eastern Sichuan Basin (ESB), emphasizing key tectonic and depositional events. Additionally, the litho-stratigraphic column highlights major petroleum elements identified in the Tailai Gas field. Stratigraphic markers corresponding to interpreted horizons are depicted in the column, ranging in age from ~720 Ma to about 160 Ma. H1: the base of the Lower Sinian Doushantuo Formation. H2: the base of the Middle Permian Liangshan Formation. H3: the base of the Upper Permian Longtan Formation. H4: the base of the Middle Triassic Leikoupo Formation; H5: the base of the Upper Triassic Xujiahe Formation; H6: The base of the second member of the Lower Jurassic Ziliujing Formation. H7: the base of the Middle Jurassic Shangshaximiao Formation.

samples with fracture-filling cements from Well TL7, and 4 samples with cements and pyrobitumen in fractures and vugs from Well TL601 (Table 1). The 11 carbonate samples were made into doubly polished thick sections of 100 μm thickness. The multi-stage dolomite, calcite and quartz cements were examined by transmitted light microscopy, cathodoluminescence (CL), and Rare Earth Elements and Yttrium (REEY) analysis. Fluid inclusion analysis, involving petrographic examination and Raman spectroscopy, was carried out to differentiate between primary and secondary inclusions, and to determine the fluid inclusion compositions. Additionally, in situ U-Pb dating of calcite cements containing

pyrobitumen and methane inclusions was conducted to establish absolute ages for the onset of oil and gas charging.

The petrographic observation of cements and fluid inclusion was conducted using a Nikon-LV100 microscope. The CL color of cements was delineated using a CL8200 MK5 CL instrument at the Wuxi Research Institute of Petroleum Geology, Petroleum Exploration and Production Research Institute, SINOPEC. Fluid inclusions were analyzed using the fluid inclusion assemblage (FIA) approach (Goldstein, 2001). Fluid inclusion Laser Raman spectrum was performed using a JY/Horiba LABRAM HR800 at the College of Marine Science and Technology, China University of Geosciences (Wuhan).

Table 1Sampling information for the carbonate samples in the third member of Maokou Formation of the Tailai Gas Field.

Sample	Well	Formation	Depth, m	Stages of cements	Host rocks
S1	TL6	Maokou Formation	5510.20	Cal-2 and Qtz	Matrix dolomite with fractures and vugs
S2	TL7	Maokou Formation	5094.70	Dol, Cal-2 and Qtz	Matrix dolomite with a fracture
S3	TL7	Maokou Formation	5101.11	Dol, Cal-2 and Cal-3	Matrix dolomite with a fracture
S4	TL7	Maokou Formation	5101.21	Dol, Cal-1 and Cal-2	Limestone with fractures
S5	TL7	Maokou Formation	5102.40	Dol and Cal-1	Limestone with fractures
S6	TL7	Maokou Formation	5105.82	Dol and Cal-2	Limestone with fractures
S7	TL7	Maokou Formation	5107.45	Cal-1 and Cal-3	Limestone with fractures
S8	TL601	Maokou Formation	5515.70	Cal-1 and Cal-3	Limestone with fractures
S9	TL601	Maokou Formation	5521.10	Dol	Matrix dolomite with fractures
S10	TL601	Maokou Formation	5527.00	Dol and Cal-2	Limestone with fractures
S11	TL601	Maokou Formation	5534.05	Dol and Cal-2	Matrix dolomite with fractures and vugs

Note: Dol: dolomite cements; Cal-1, Cal-2, Cal-3: the first, second, third stage of calcite cements, respectively; Qtz: quartz cements.

The Laser Raman spectrum of pyrobitumen inclusions was conducted using a 300-gr.mm-1 grating, with the output power of 150 mW. The Laser Raman spectrum of gas inclusions was respectively measured using 300-gr.mm-1 and 1800-gr.mm-1 grating, with the output power of 300 mW.

The REEY analysis and in situ U-Pb dating of calcite cements were performed using a Laser Ablation Inductively Coupled Plasma Mass Spectrometer (LA-ICP-MS) at the Guizhou Tongwei Analytical Technology Co., Ltd. The LA-ICP-MS is a RESOlution SE-S155 Laser Ablation System coupled with a Thermo Fisher iCAP RQ ICP-MS. For REEY analysis, the laser spot, frequency, and fluence were set at 100 μm, 10 Hz, and 3 J/cm², respectively. Sample points were preablated 20 times to eliminate potential surface contamination. The experimental procedure for each sample comprised a 15 s background, a 20 s ablation, and a 10 s washout time. The laserablated sample was carried out of the sample cell by helium, mixed with argon, and then entered the ICP-MS to complete the REEY analysis. NIST614 was used as the internal standard for data calibration. Background selection and data calculation were performed using IOLITE version 3.71 software (Paton et al., 2011). The REEY contents of the host rocks and veins were normalized to Post-Archaean Australian Shale (PAAS) compositions (McLennan, 1989).

The radiometric U-Pb dating of calcite containing primary and secondary pyrobitumen/oil/gas inclusions has been recently applied to determine the absolute ages of oil/gas charging in hydrocarbon fields (Chen et al., 2022). Sample preparation proceeded as follows: 1) calcite samples were made into standard 2.5-cmdiameter mounts with epoxy resin; 2) mounts were cleaned with ultrasound and ultrapure water (MQ) to eliminate surface contamination 0.3) dried mounts were assembled into the sample holder. Before performing in situ U-Pb dating, the laser spot, frequency, and fluence were respectively set at 120 µm, 15 Hz, and 2.5 I/cm². All points to be measured were pre-ablated 15 times to remove potential surface contamination. The experimental procedure comprised a pre-ablation background of 15 s, an ablation period of 20 s, and a washout time of 5 s. The sample ablated by laser was carried out of the sample cell by helium, mixed with argon, and then entered the ICP-MS for isotopic measurements. Our samples were measured together with a NIST 614 glass standard and several matrix-matched laboratories working calcite standards, such as AHX-1d and PTKD-2 (Pan et al., 2021; Kendrick et al., 2022; Ni et al., 2024b). Repeated measurements of the NIST 614 glass and calcite standards were used to correct for ²⁰⁷Pb/²⁰⁶Pb fractionation and instrument-related drift in the ²⁰⁶Pb/²³⁸U ratios. In-house carbonate standard AHX-1d with a cross-calibrated age of 238.2 ± 1.0 Ma was used for bias corrections of the measured 238 U/ 206 Pb ratios. We adopted the built-in "U-Pb geochronology" data reduction schemes (DRS) embedded in the IOLITE package of Paton et al. (2011) to calculate U-Pb isotope ratios, apparent U-Pb ages, and U-Th-Pb concentration calculations. Later, the data were regressed on the Tera-Wasserburg concordia plots using the ISO-PLOT version 3.75 of Ludwig (2012) to determine each sample's U-Pb age (Chen et al., 2022).

The maturity history of source rocks in the Qiongzhusi Formation, Wufeng-Longmaxi Formation, and the first member of the Maokou Formation was modeled using BasinMod-1D® software, based on reconstructed burial and thermal histories. Parameters such as lithology, stratigraphic thickness, measured maturity data, and borehole temperatures were provided by SINOPEC. Absolute ages and erosional thickness were acquired from Deng et al. (2009) and He et al. (2011). The burial history was reconstructed using the back-stripping method, incorporating lithology, ages of tectonic episodes, and stratigraphic and erosional thicknesses (He and Middleton, 2002). Present-day heat flow values were calculated from the thermal conductivity of rock units and geothermal gradients as determined from the measured borehole temperatures. Porosity was calculated by the initial porosity and reciprocal porosity reduction method from the BasinMod-1D® software. Paleo-heat flow values for the ESB from Jiang et al. (2018) and Qiu et al. (2022) were used to simulate the thermal history in the study area. The source rocks in the Qiongzhusi Formation, Wufeng-Longmaxi Formation, and the first member of the Maokou Formation were considered as the main source intervals in this study. The kerogen types of the source rocks in the Qiongzhusi Formation and Wufeng-Longmaxi Formation are sapropelic, while the kerogen type of source rock in the first member of the Maokou Formation is humic-sapropelic (Zou et al., 2014; Li et al., 2021). The basin modeling results were calibrated by the measured borehole temperatures and maturity data.

3D seismic data were used to interpret the structural style and reactivation history of the No. 15 Fault System, including the associated faults, over multiple tectonic episodes. The interpreted 3D seismic data in the Tailai Gas Field cover an area of approximately 1500 km², with a sampling interval of 1 ms and a bin spacing of 20 m \times 20 m. Vertical resolution can reach 25 m. During seismic interpretation, 7 regional stratigraphic horizons were interpreted and dated based on previous studies in the Sichuan Basin (e.g., Zhang et al., 2020; Gu et al., 2021). The variance seismic attribute cube of the 3D seismic data was calculated using Schlumberger's Petrel®. In this study, the variance attribute was used to study the plan-view characteristics of the No. 15 Fault System. In the variance maps, faults are detected through variations between seismic traces, which were depicted with a high variance coefficient. The variance seismic attribute quantifies the disparities among seismic traces, transforming a continuous volume into a discontinuous one, thereby emphasizing structural and stratigraphic boundaries (Omosanya, 2018, 2020). Moreover, seismic profiles were interpreted to analyze the geometry and structural

style of the No. 15 Fault System and its splayed segments. Thickness changes of strata may record the reactivation periods of a given fault (Shiroodi et al., 2015). The thickness changes of strata across the No. 15 Fault system were applied to understand its growth history vis-a-vis propagation, reactivation and segmentation (Omosanya et al., 2015).

4. Results

4.1. Petrography

Fractures were widely developed in the 11 carbonate samples, with some vugs observed in the third member of the Maokou Formation (Table 1). The fractures in the core samples are predominantly low-angle (34°-45°) or high-angle structures (62°-90°). Low-angle fractures are 1-21 mm in width and filled with dolomite, calcite, and quartz. High-angle fractures show a relatively narrower width (2-17 mm) and are also filled with dolomite, calcite, and quartz. Dissolved vugs were semi- or fully filled with dolomite and calcite cements. The dolomite (Dol), calcite (Cal), and guartz (Qtz) cements in the HDR samples can be divided into five stages, represented by Dol cements (stage 1), Cal-1 cements (stage 2), Cal-2 cements (stage 3), Cal-3 cements (stage 4), and Qtz cements (stage 5). The Dol cements are characterized by coarse-grained dolomite with multiple cracks and a pink CL color (Fig. 3(a1) and (a2)). The diagenetic fluid of the Cal-1 cements with dark orange CL color dissolved euhedral Dol cements, suggesting that the Cal-1 cements were formed later than the Dol cements (Fig. 3(a1) and (a2)). Cal-2 cements with dark orange CL color developed in the fractures and cut through the Cal-1 cements, indicating that Cal-2 cements are later than Cal-1 cements (Fig. 3(a1) and (a2)). Cal-3 cements with bright orange CL color precipitated in the fractures within the Cal-1 cements and should be formed from a later fluid postdating the Cal-1 cements (Fig. 3(b1) and (b2)). In situ U-Pb dating of Cal-2 and Cal-3 cements confirm that the Cal-3 cements are later than the Cal-2 cements. The latest stage Qtz cements are characterized by coarse-grained quartz with a dark CL color (Fig. 3(c1) and (c2)).

4.2. REEY and elements composition

The REEY distribution patterns and anomalies can be used to effectively distinguish different stages of calcite cements (Robbins et al., 2016). PAAS-normalized REEY patterns of the three stages of calcite cements from the HDR in the third member of the Maokou Formation are presented in Fig. 4. The three-stage calcite cements have different REEY characteristics, with distinct negative Ce anomalies and weak Eu anomalies in the Cal-1 cements, distinct negative Ce anomalies and pronounced positive Eu anomalies in the Cal-2 cements, negative Ce anomalies and weak positive Eu anomalies in the Cal-3 cements.

The Cal-1 cements exhibit distinct negative Ce anomalies ($\delta Ce = 0.19 - 0.31$) and weak Eu anomalies ($\delta Eu = 0.95 - 1.78$) (Fig. 4(a) and Table A-1). REEY patterns of Cal-2 cements show negative Ce anomalies ($\delta Ce = 0.16 - 0.27$) and distinct positive Eu anomalies ($\delta Eu = 4.40 - 36.47$), and reveal a notable depletion in HREE relative to MREE with their Tb/Yb ratios ranging from 3.03 to 13.41 (Fig. 4(b) and Table A-1). The Cal-3 cements have weak negative Ce anomalies ($\delta Ce = 0.38 - 0.75$) and weak positive Eu anomalies ($\delta Eu = 1.10 - 2.32$) (Fig. 4(c) and Table A-1). The δCe values of the Cal-3 cements are higher than those of the Cal-1 and Cal-2 cements (Table A-1), indicating different geochemical

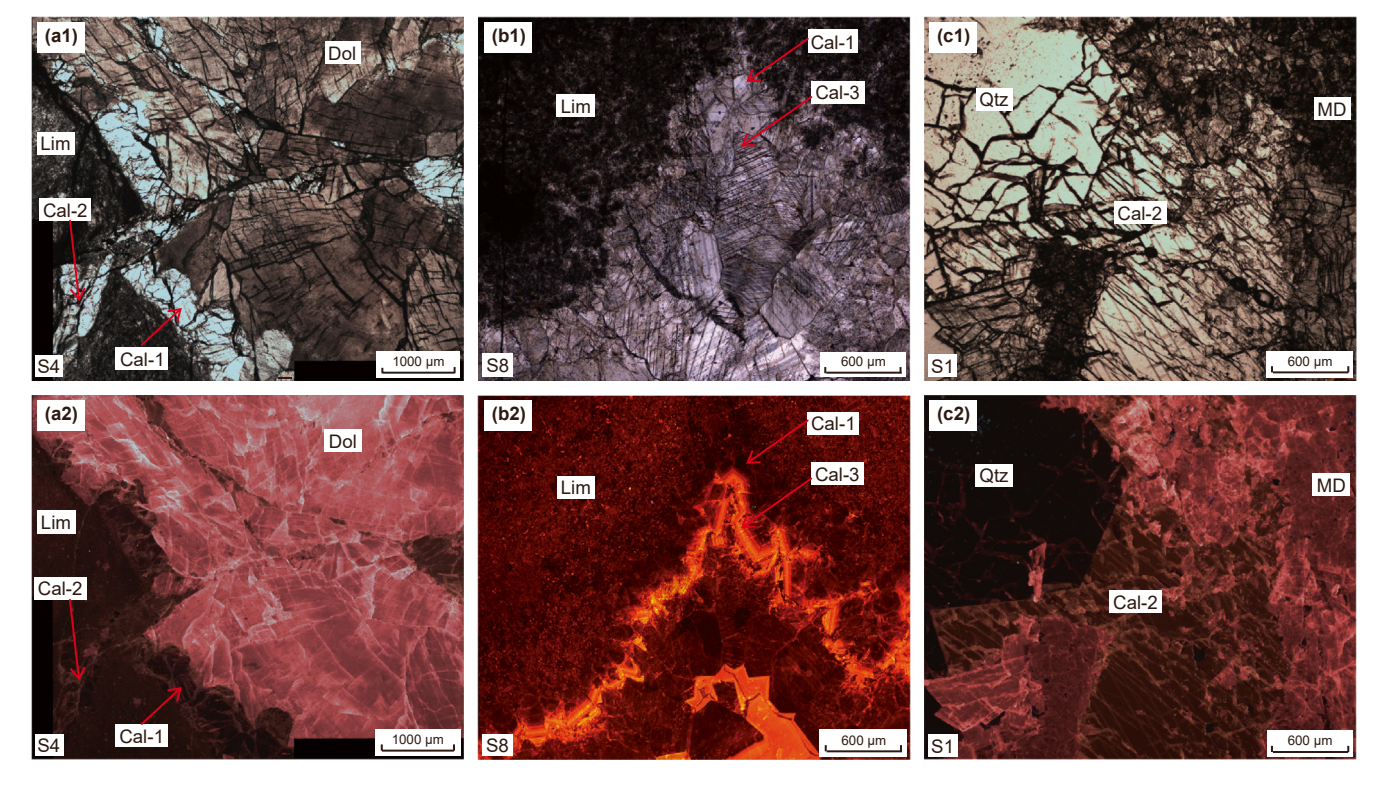
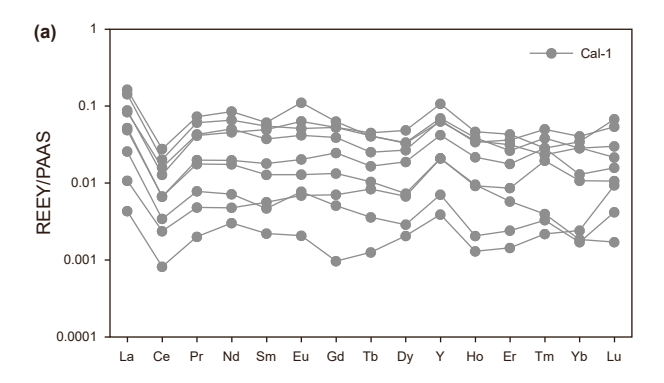
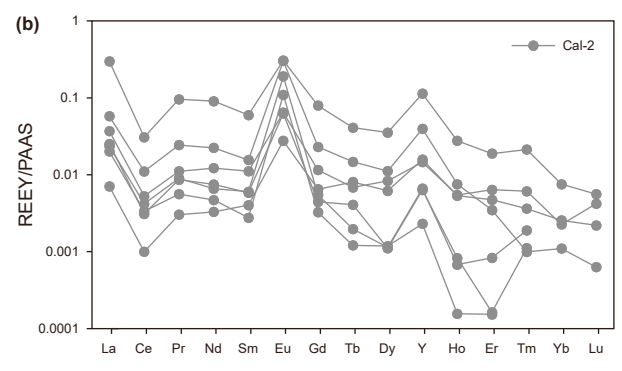


Fig. 3. Plane-polarized light (PPL) and cathodoluminescence (CL) photomicrographs of the carbonate samples in the Middle Permian Maokou Formation in the Tailai Gas Field. (a1) and (a2): PPL and CL photomicrographs show that the Dol cements are characterized by pink CL color, and Cal-1 and Cal-2 cements are characterized by dark orange CL color. (b1) and (b2): PPL and CL photomicrographs show that Cal-3 cements are characterized by bright orange CL color. (c1) and (c2): PPL and CL photomicrographs show that Qtz cements are characterized by dark CL color. Lim: Limestone; MD: Matrix dolomite; Dol: dolomite cements; Cal-1, Cal-2, Cal-3: the first, second, third stage of calcite cements, respectively; Qtz: quartz cements.





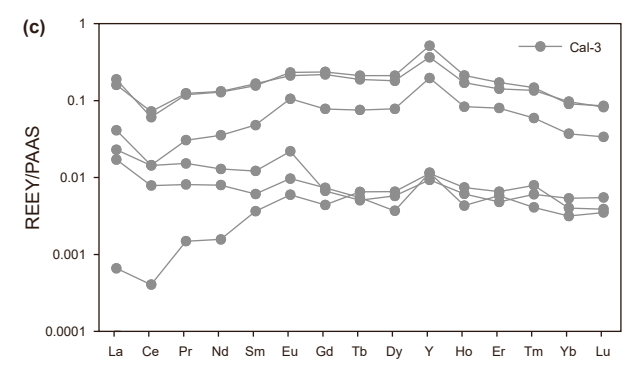


Fig. 4. Distributions of REEY in the calcite cements (Cal-1, Cal-2, Cal-3 cements) from the Tailai Gas Field (the third member of the Maokou Formation). **(a)**: REEY patterns of the Cal-1 cements. **(b)**: REEY patterns of the Cal-2 cements. **(c)**: REEY patterns of the Cal-3 cements. The concentrations shown are normalized to Post-Archaean Australian Shale (PAAS) (McLennan, 1989).

characteristics for Cal-3 cements compared to Cal-1 and Cal-2 cements. The Cal-3 cements also exhibit a slight deficit in HREE compared to the MREE with their Tb/Yb ratios ranging from 0.94 to 2.33. Different REEY patterns of the calcite cements from the HDR in the third member of the Maokou Formation indicates that three-stage calcite cements have different geochemical characteristics and cement-forming fluid origins.

4.3. Fluid inclusions

Calcite cements from the hydrothermal dolomite reservoirs (HDR) in the Tailai Gas Field contain abundant fluid inclusions, predominantly pyrobitumen and single-phase gas inclusions (Fig. 5). Primary inclusions were trapped on the growing face of the host crystal during their precipitation, while secondary inclusions were trapped in crystal cracks after the formation of the host mineral (Chi et al., 2021). Primary inclusions are particularly observed in the three-stage calcite cements (Fig. 5). In the Cal-1 cements, primary pyrobitumen inclusions are isolated inside the

crystals and appear as circles in shape and 2–10 μm in size (Fig. 5(a)). The Cal-2 cements consist of primary and secondary single-phase gas inclusions. The primary single-phase gas inclusions are isolated, with diameters ranging from 3 to 14 μm , showing elliptical and square shapes (Fig. 5(b)). The secondary single-phase gas inclusions align along crystal cracks, with diameters varying from 3 to 10 μm and exhibiting rectangular, elliptical, and square shapes (Fig. 5(c)). Primary single-phase gas inclusions in the Cal-3 cements are directionally distributed inside the crystals, with diameters ranging from 3 to 11 μm and appearing in triangular and square shapes (Fig. 5(d)).

Laser Raman spectra of primary pyrobitumen inclusions in the Cal-1 cements are shown in Fig. 6(a). Two first-order characteristic bands, namely the D and G bands, are revealed in Fig. 6(a). The positions of the D and G bands appear respectively at Raman Shift values of 1314.54–1326.41 cm⁻¹ and 1584.57–1596.44 cm⁻¹ with a 300 gr.mm⁻¹ grating. Laser Raman spectra of the primary single-phase gas inclusion in the Cal-2 cements show the Raman peak shift of CH₄, with values ranging from 2910.93 to 2916.91 cm⁻¹ with a 300 gr.mm⁻¹ grating (Fig. 6(b)). Laser Raman spectra of secondary single-phase gas inclusions within the Cal-2 cements also show the Raman peak shift of CH₄, with values of 2911.01–2913.09 cm⁻¹ with an 1800 gr.mm⁻¹ grating (Fig. 6(c)). Laser Raman spectra of the primary single-phase gas inclusion in the Cal-3 cements show typical Raman peak shift of CH₄, with a value of approximately 2916.91 cm⁻¹ with a 300 gr.mm⁻¹ grating (Fig. 6(d)).

4.4. U-Pb geochronology

In situ U-Pb dating was successfully performed on the Cal-1, Cal-2 and Cal-3 cements, as well as the standard sample AHX-1d. The high ²³⁸U/²⁰⁶Pb ratios of in these samples yielded robust U-Pb age regressions (Fig. 7). The U and Pb contents of the Cal-1 cements from sample T8 range from 0.002 ppm to 1.764 ppm and 0.010 ppm - 0.104 ppm, respectively. The high $^{238}\text{U}/^{206}\text{Pb}$ ratios and low ²⁰⁷Pb/²⁰⁶Pb ratios of the Cal-1 cements generated a reliable age of 246.9 \pm 4.8 Ma (MSWD = 0.74; Fig. 7(a)). The U contents of the Cal-2 cements from sample T11 vary from 0.005 ppm to 1.310 ppm, with low concentrations of Pb (0.015–0.331 ppm). The wide range of ²³⁸U/²⁰⁶Pb ratios and corresponding ²⁰⁷Pb/²⁰⁶Pb ratios of the Cal-2 cements yielded a precise age of 222.4 \pm 8.6 Ma (MSWD = 1.7; Fig. 7(b)). The U and Pb concentrations of the Cal-3 cements from sample T8 vary from 0.002 ppm to 0.286 ppm and 0.007 ppm-0.034 ppm, respectively. The ²³⁸U/²⁰⁶Pb ratios and corresponding ²⁰⁷Pb/²⁰⁶Pb ratios yielded an accurate age of 175.2 ± 7.7 Ma for the Cal-3 cements (MSWD = 2.0; Fig. 7(c)).

4.5. Modelling of the burial history and hydrocarbon generation history

The thermal history was reconstructed based on present-day and paleo-heat flow values in this region. The average geothermal gradient for well TL6 is 21.36 °C/km, calculated using measured borehole temperatures from drill-stem tests (DSTs) and an average present-day surface temperature of 15 °C. The present-day heat flow value for well TL6 is estimated as 51.35 mW/m² using the transient heat flow method according to its geothermal gradient. Paleo-heat flow values during the Cambrian-Quaternary of the wells around the Tailai Gas Field were calculated using apatite fission track (AFT) and vitrinite reflectance (Jiang et al., 2018; Qiu et al., 2022). The reconstructed thermal history of well TL6 show that the paleo-heat flow was stable from the Cambrian to the early Carboniferous, with values ranging from 48 to 55 mW/m² in the Tailai Gas Field. The heat flow gradually increased during the Hercynian orogeny, reaching its highest value of approximately

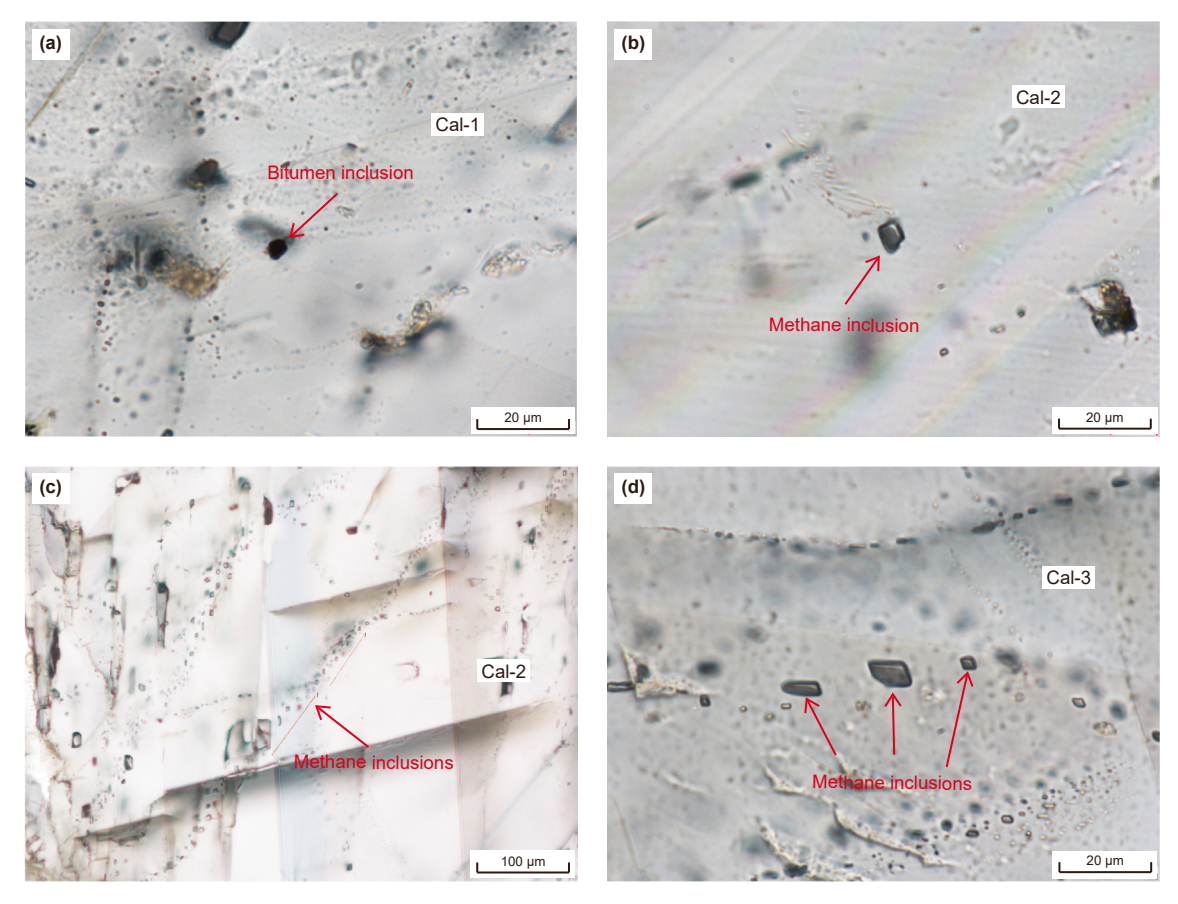


Fig. 5. Photomicrographs of primary and secondary fluid inclusions in the calcite cements from the third member of the Maokou Formation in the Tailai Gas Field. (a): Primary pyrobitumen inclusions in Cal-1 cements from sample S8. (b): Primary single-phase gas inclusions in Cal-2 cements from sample S11. (c): Secondary single-phase gas inclusions in Cal-2 cements from sample S2. (d): Primary single-phase gas inclusions in Cal-3 cements from sample S8.

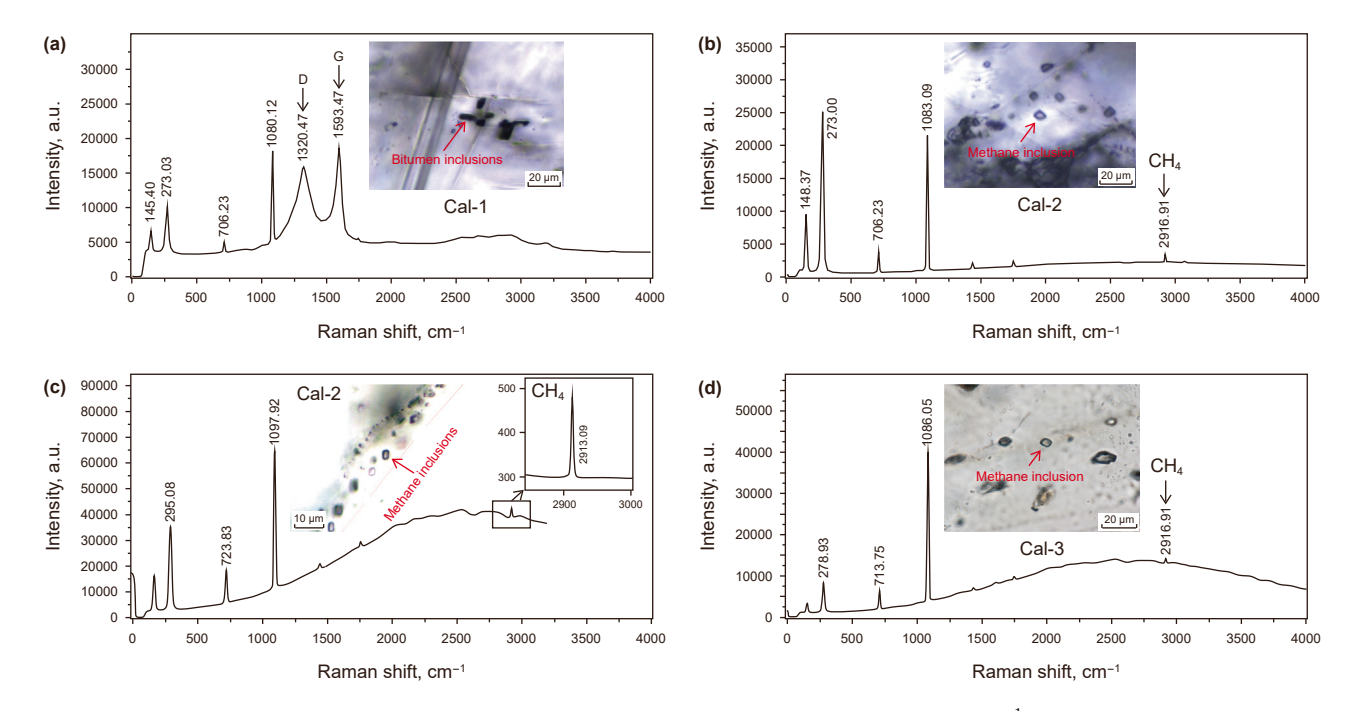


Fig. 6. Laser Raman spectra of pyrobitumen inclusions and pure methane inclusions in various samples collected with 300 gr.mm⁻¹ grating. (a): Primary pyrobitumen inclusions within Cal-1 cements, with 300 gr.mm⁻¹ grating. (b): Primary single-phase methane inclusions within Cal-2 cements, with 300 gr.mm⁻¹ grating. (c): Secondary single-phase methane inclusions within Cal-2 cements, with 300 gr.mm⁻¹ grating. (d): Primary single-phase methane inclusions within Cal-3 cements, with 300 gr.mm⁻¹ grating.

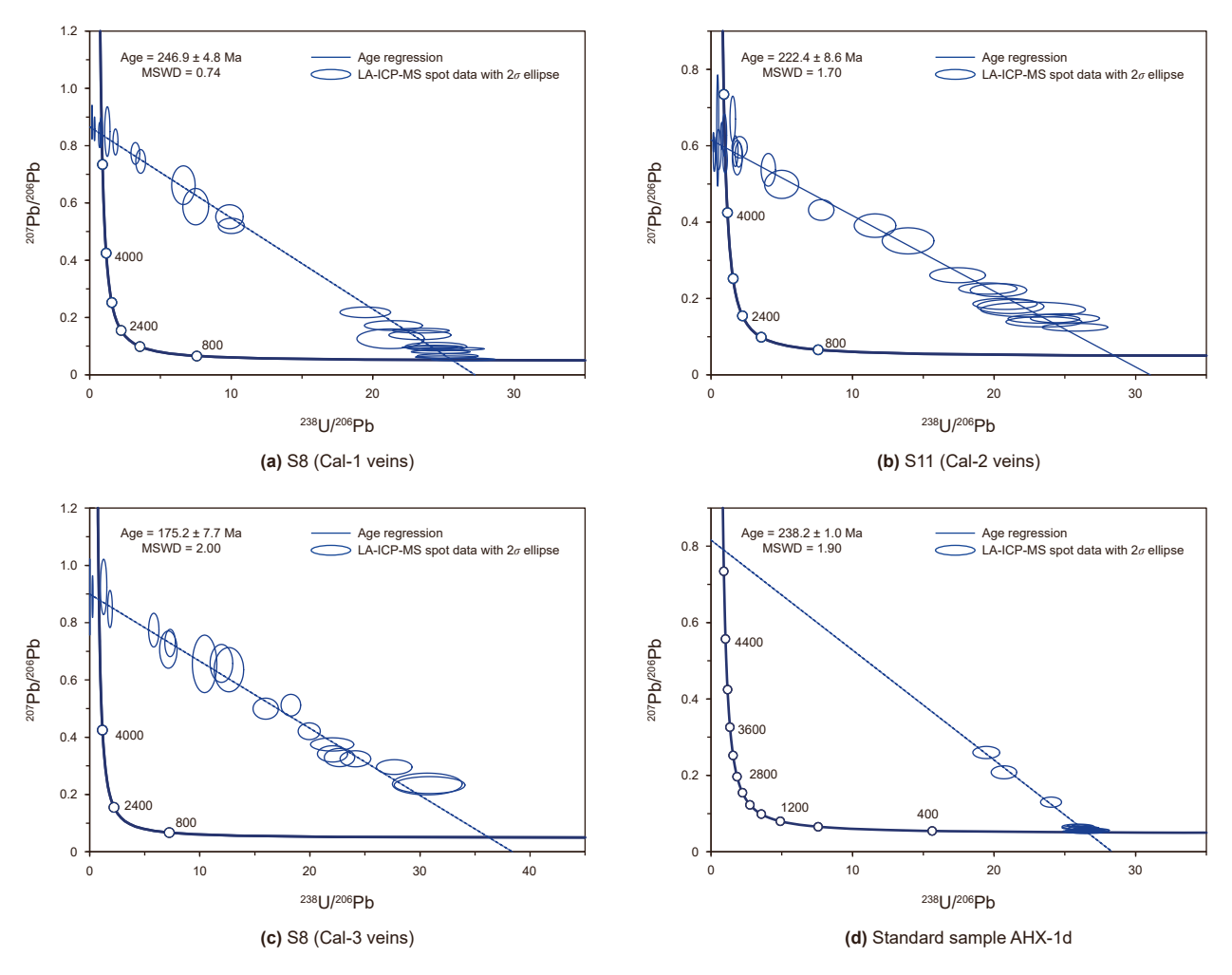


Fig. 7. U-Pb Tera-wasserburg Concordia plots for calcite samples taken from HDR in the Tailai Gas Field (the third member of the Maokou Formation) and the standard sample AHX-1d. MSWD: mean square of weighted deviates; LA-ICP-MS: laser ablation-inductively coupled plasma-mass spectrometer.

70 mW/m² in the Late Permian (about 259 Ma), corresponding to the formation of the Emeishan Large Igneous Province (Jiang et al., 2018). The heat flow then quickly decreased until the Early Jurassic, from which point the heat flow slowly decreased to the modern

value of 51.35 mW/m² (Fig. 8(a)). The excellent correlation among modeled maturity and temperature, measured vitrinite reflectance, and borehole temperature values from well TL6 (Fig. 8(b)) supports that the thermal history model of well TL6 is accurate.

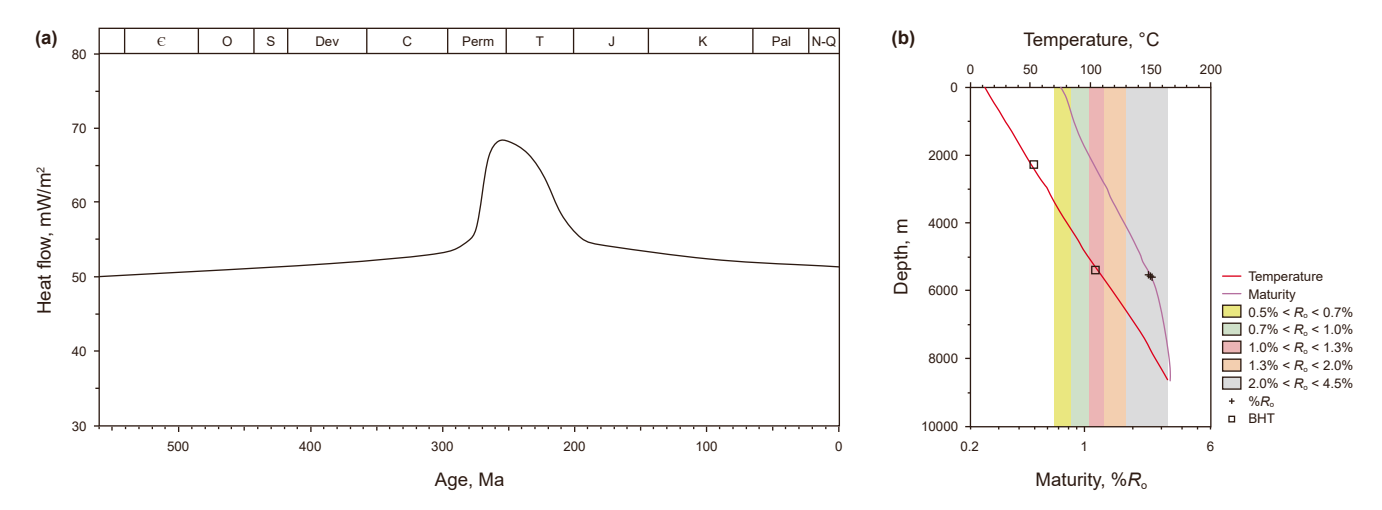


Fig. 8. (a): The thermal history of well TL6 in the Tailai Gas Field in the ESB; (b): Correlation among modeled maturity and temperature evolution and measured vitrinite reflectance values and temperatures from well TL6.

Burial curves for well TL6 show that the study area experienced subsidence from the Cambrian to the Late Silurian, and long-term uplift and denudation during the Devonian and the Carboniferous. The study area continued to subside during the Middle Permian and experienced slight uplift at the end of the Middle Permian, owing to the Dongwu movement, Rapid and slow subsidence respectively occurred during the Late Permian-Middle Triassic and the Late Triassic. The study area underwent a slight uplift during the Triassic corresponding to the Indosinian orogeny. Subsequently, the strata experienced long-term subsidence and reached their maximum burial depths during the early Cretaceous (around 110 Ma) in the study area. This was followed by rapid uplift and denudation at the end of the early Cretaceous corresponding to the Yanshanian orogeny, gradual and slow uplift from the late Cretaceous to the Paleogene, and rapid uplift and erosion during the Himalayan orogeny from the Neogene to the present day (Fig. 9, Wang et al., 2022).

The maturity history of the Qiongzhusi Formation source rock revealed that it reached the hydrocarbon generation window around 445 Ma (Fig. 10(a)). The Qiongzhusi Formation source rock was in the early-mature stage $(0.5\%< R_0<0.7\%)$ from 445 to 421 Ma, then entered the middle-mature stage $(0.7\%< R_0<1.0\%)$ from 421 to 264 Ma. The Qiongzhusi Formation source rock reached the stage of massive oil generation with Ro values ranging from 1.0% to 1.3% between 264 and 252 Ma, subsequently approached the stage of wet gas generation $(1.3\%< R_0<2.0\%)$ from 252 to 245 Ma, and finally entered the over-mature stage $(2.0\%< R_0<4.5\%)$ from 245 to 135 Ma (Fig. 10(a)). The maturity of the Wufeng-Longmaxi Formation source rock reached 0.5% at about 406 Ma, approached 0.7% around 248 Ma, and rapidly increased to 1.0% at approximately 245 Ma (Fig. 10(b)). The Wufeng-Longmaxi Formation source rock reached the peak of oil generation with R_0 values ranging from 1.0% to 1.3%

between 245 and 229 Ma. The Wufeng-Longmaxi Formation source rock was in the stage of wet gas generation (1.3%< R_0 <2.0%) from 229 Ma to 160 Ma, and then entered the over-mature stage (2.0%< R_0 <4.5%) since 160 Ma (Fig. 10(b)). The maturity of the source rock in the first member of the Maokou Formation reached 0.5% at about 247 Ma and rapidly increased to 0.7% around 235 Ma. The source rock in the first member of the Maokou Formation was in the middle-mature stage (0.7%< R_0 <1.0%) from 235 to 165 Ma, reached the late-mature stage from 165 to 160 Ma (1.0%< R_0 <1.3%), entered the stage of wet gas generation (1.3%< R_0 <2.0%) from 165 to 148 Ma, and finally approached the over-mature stage since 148 Ma (Fig. 10(c)).

4.6. Structural characteristics of the no. 15 fault system

The No. 15 Fault System includes strike-slip basement faults, with a northwest-southeast orientation (Li et al., 2023). Segmentation of the No. 15 Fault System is evident from the variance time slice at a depth of –2505 ms TWT. Fig. 11 shows that the No. 15 Fault System consists of nine fault segments with lengths ranging from 3.57 to 8.82 km in the Tailai Gas Field. Fault segments 1, 2, 3, 4, 5, and 9 exhibit curvilinear structures with azimuths ranging from 298° to 351°, while fault segments 6, 7, and 8 display braided structures with azimuths varying from 315° to 323° (Fig. 11). Fig. 12 further reveals that the No. 15 Fault System was developed mostly beneath the Lower Triassic evaporite layer, and the supra-evaporite faults were associated faults.

Consequently, four seismic profiles perpendicular to fault segments 6, 7, 8, and 9 were selected for detailed interpretation and structural analysis. The No. 15 Fault System can be categorized into two groups of faults based on its stratified characteristics on the profiles (Fig. 12). Faults in Group 1 offset the Lower Triassic

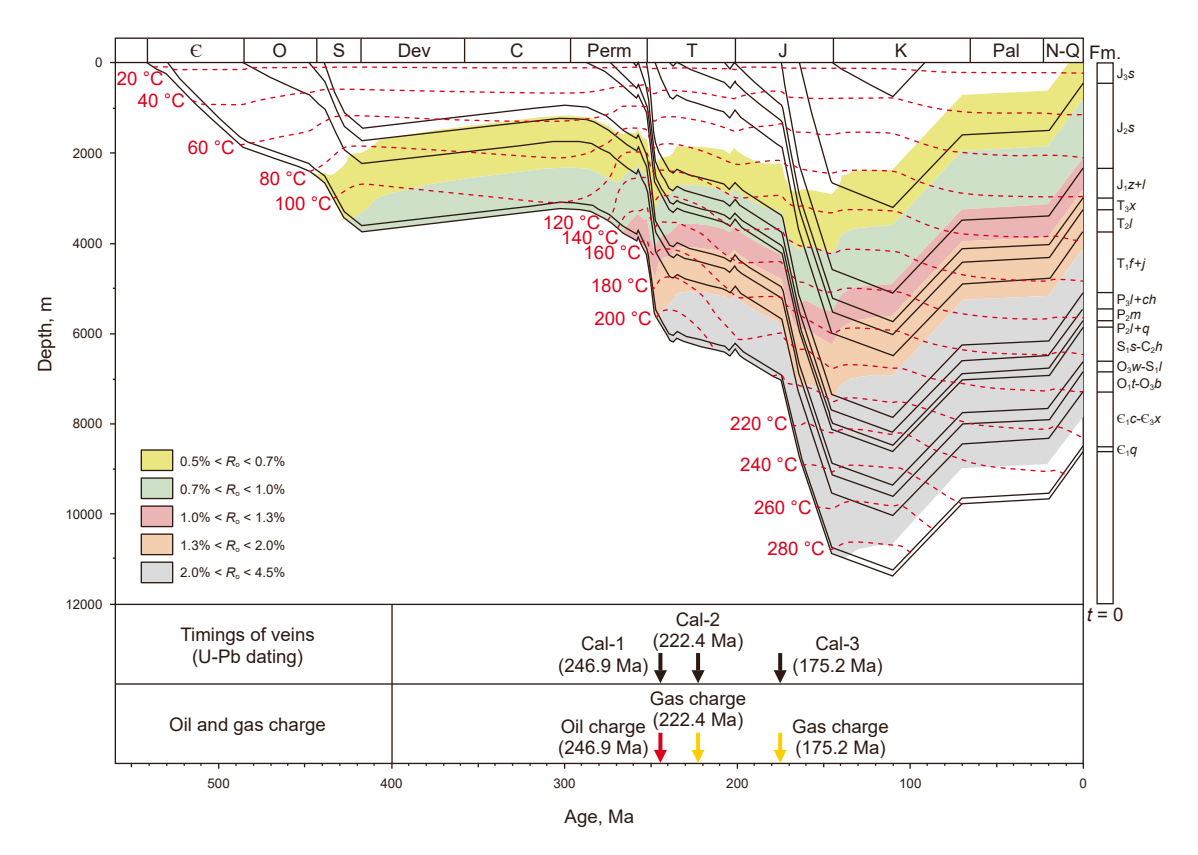
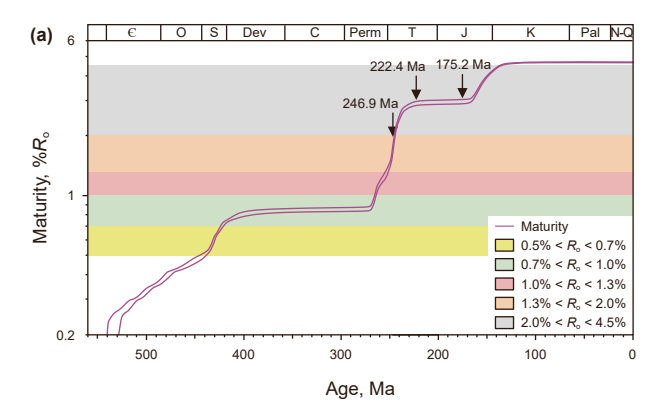
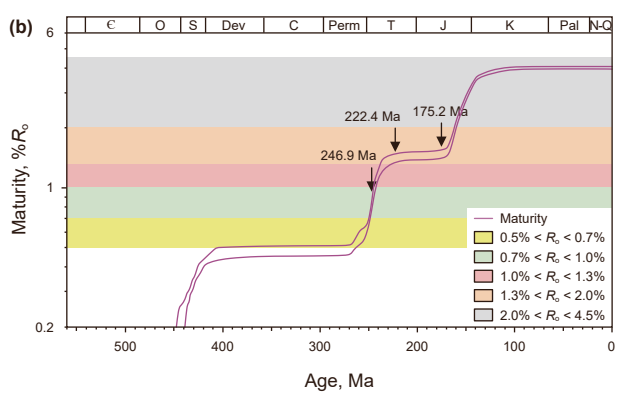


Fig. 9. Burial and thermal history models for well TL6, including information on the timings of calcite vein formation and hydrocarbon charging.





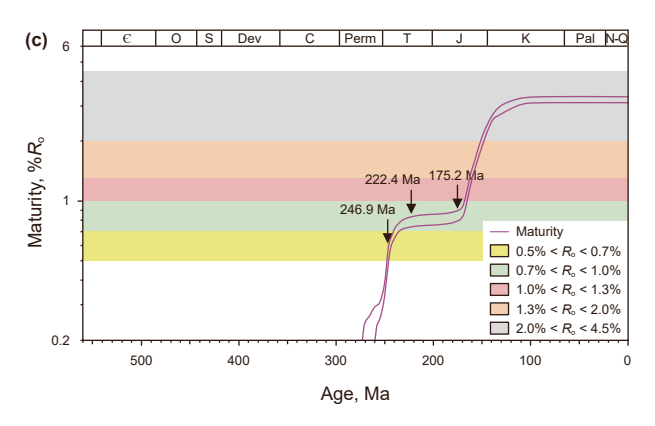


Fig. 10. Simulation of the maturity history of the source rock in the Lower Cambrian Qiongzhusi Formation (a), Ordovician-Silurian Wufeng—Longmaxi Formations (b), and the first member of Middle Permian Maokou Formation (c) in the ESB. 246.9 Ma: the time of the first episode of oil charge into the Middle Permian Maokou Formation; 222.4 Ma: the time of the first episode of gas charge into the Middle Permian Maokou Formation; 175.2 Ma: the time of the second episode of gas charge into the Middle Permian Maokou Formation.

evaporite layer (Fig. 12). Group 2 faults are primarily defined by the base of the Middle Triassic Leikoupo Formation (Horizon H4) and the Upper Triassic Xujiahe Formation (Horizon H5). The upper tips of faults in Group 1 terminate at the Lower Triassic evaporite layer (Fig. 12). Within Group 1, fault segment 6 includes a positive flower structure (Fig. 12(a)). Fault segment 7 consists of a vertical fault and a negative flower structure (Fig. 12(b) and (c)). Fault segment 8 is composed of a semi-flower structure and a negative flower structure (Fig. 12(d)). The structural style of fault segment 9 is a positive flower structure with small dip slips (Fig. 12(c)). Group 2 comprises numerous normal and reverse faults with high dip angles beneath Horizon H5, with their lower tips ending at the Lower Triassic evaporite layer.

5. Discussion

5.1. Fault activation in the Tailai Gas Field

The No. 15 Fault System was formed during the Xingkai taphrogenesis (Gu and Wang, 2014; Su et al., 2020). The No. 15 Fault System underwent multi-stage reactivation due to the subsequent tectonic movements, as indicated by vertical displacement and lateral throw distribution along the fault system (Li et al., 2023). Shiroodi et al. (2015) proposed that these reactivation events are preserved in thickness variations of identical strata across the fault system.

The Middle Permian strata adjacent to the No. 15 Fault System exhibit minor thickness variations, thinning along fault segment 6 and thickening along fault segment 7 (Fig. 13(a)). In cross-section, the No. 15 Fault System displays a ribbon-like structure, characterized by vertical strike-slip faults and both positive and negative flower structures in Group 1 (Fig. 12). This indicates that the No. 15 Fault System experienced strike-slip movement during the Middle Permian, consistent with the Dongwu tectonic event. Fig. 13(b) shows that multiple sea troughs were developed in Middle Triassic Leikoupo Formation within the No. 15 Fault System, likely controlled by bounding normal faults (Fig. 12(c)). These troughs are characterized by significant thickening of the Leikoupo Formation (Fig. 13(b)). This suggests that the No. 15 Fault System underwent transtensional deformation during the Middle Triassic, coinciding with the early stage of the Indosinian orogeny. Subsequently, boundary normal faults of the sea troughs were inverted to reverse faults, forming Group 2 faults (Figs. 12 and 13(b)). This suggests that the formation of these reverse faults postdated to the development of the sea troughs. Faults in group 2 are bounded by the base of the Leikoupo Formation (Horizon H4) and the Xujiahe Formation (Horizon H5) (Fig. 12), indicating that these faults formed prior to Formation deposition during the (208.5–201.4 Ma; Tong et al., 2019). This structural inversion and associated fault reactivation likely occurred during the Late Triassic, triggered by compressional stresses in the late stage of the Indosinian orogeny (Harrowfield and Wilson, 2005). The interval from the second member of the Ziliujing Formation to the Xiashaximiao Formation displays a blind anticline and reduced thickness within the No. 15 Fault System (Figs. 12 and 13(c)). This sequence, deposited from the Pliensbachian to Oxfordian (192.9–154.8 Ma; Huang, 2019; Peng et al., 2022), suggests that the blind anticline formation and associated fault reactivation were likely driven by compressional stresses in the early stage of the Yanshanian orogeny (Shi et al., 2016; Zheng et al., 2019). In summary, the No. 15 Fault System experienced reactivation and development during the Dongwu movement (Permian), the early and late stages of the Indosinian (Middle Triassic and Late Triassic, respectively), and the early stage of the Yanshanian (Early Jurassic) orogeny.

5.2. Hydrocarbon charging time

This study determines the timing of oil and gas charging into the HDR of the Maokou Formation using in situ U-Pb dating of calcite cements containing pyrobitumen and methane inclusions. The earliest episode involved oil. The presence of primary pyrobitumen inclusions trapped within the Cal-1 cements, which were precisely dated as 246.9 \pm 4.8 Ma (Middle Triassic), signifies that oil emplacement either coincided with or slightly predated the formation of the Cal-1 cement. This initial charging event is convincingly coupled with the reactivation of the No. 15 Fault System during the early stage of Indosinian orogeny. The reactivated fault system served as a proficient conduit, enabling oil to migrate and fill the reservoir around 246.9 Ma.

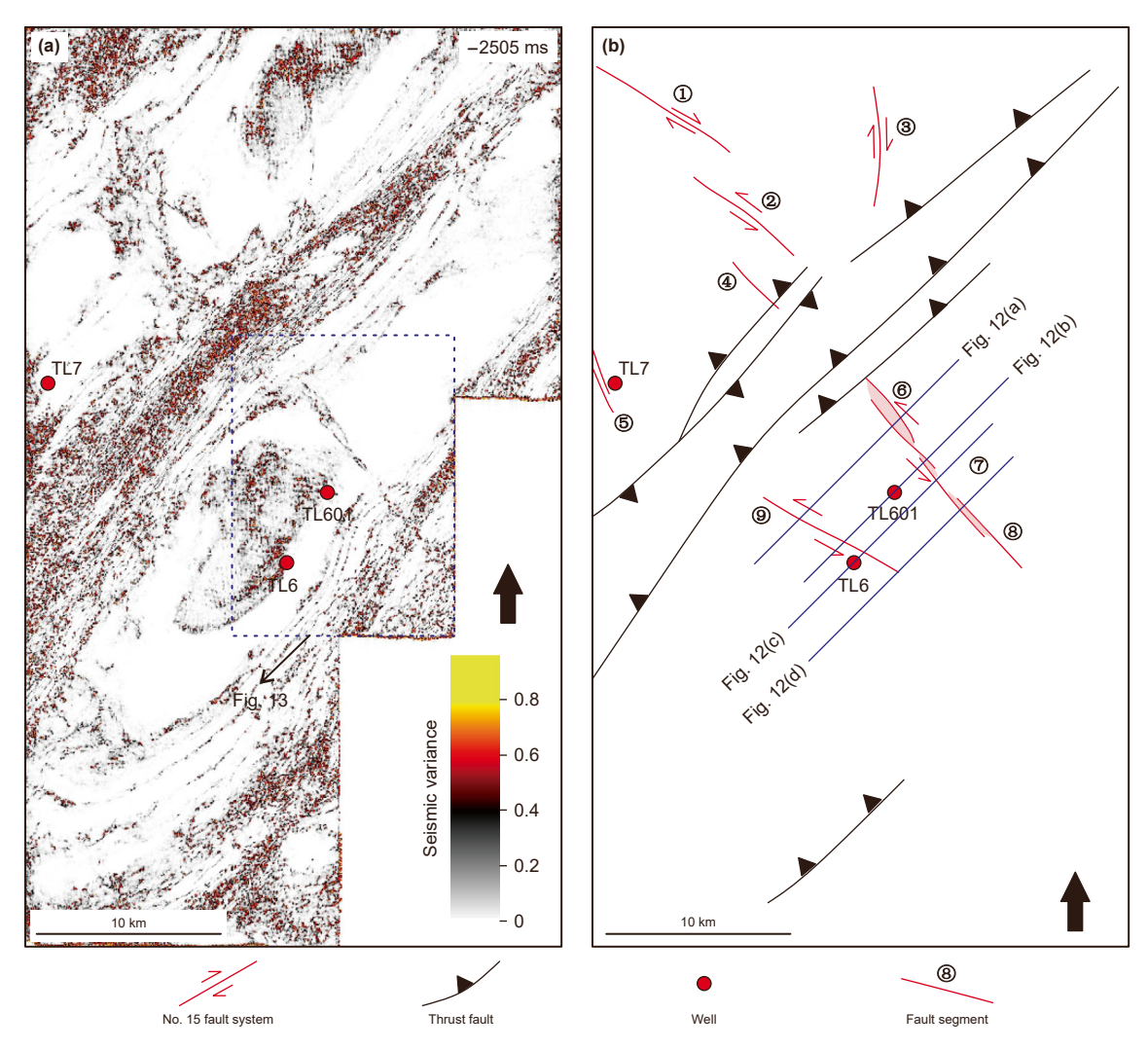


Fig. 11. Seismic variance of the Seismic data (TWT = -2505 ms) showing that the No. 15 Fault System strikes from NW to SE. ①—⑨: fault segment 1-9.

Subsequently, hydrocarbon influxes into the HDR in the third member of the Maokou Formation were dominated by methane gas (Fig. 5(b)). The first gas charging episode is manifested by primary single-phase methane inclusions within the Cal-2 cements, dated as 222.4 ± 8.6 Ma (Late Triassic). This temporal association strongly suggests a link between this gas influx and the pull-apart activity experienced by the No. 15 Fault System during the late stages of the Indosinian orogeny. The tectonic activity is inferred to have reopened the fault system, promoting migration of the methane.

A second, distinct gas charge event is unveiled by the presence of secondary single-phase methane inclusions along the crystal cracks of the Cal-2 cements and the primary methane inclusions within the Cal-3 cements (dated as 175.2 ± 7.7 Ma, Early Jurassic). This episode clearly postdated the formation of the Cal-2 cements, likely occurring either synchronously with or slightly before the precipitation of the Cal-3 cements. The reactivation of the No. 15 Fault System due to the compressive stress of the early Yanshanian orogeny is postulated as the driving force behind this event (Fig. 13(c); Shi et al., 2016; Zheng et al., 2019). The coincidence between the fault reactivation and the second gas charging episode supports this postulation. The comprehensive analysis of secondary methane inclusions along crystal cracks of the Cal-2 cements, the formation time of the Cal-3 cements with the development of the primary methane inclusions, and the reactivation of the No. 15 Fault

System during the early stage of Yanshanian orogeny consistently indicate that the second episode of gas charging occurred around 175.2 Ma.

Three episodes of hydrocarbon charging occurred in the HDR in the third member of the Maokou Formation, including one episode of oil charging around 246.9 Ma, and two episodes of gas charging at about 222.4 Ma and 175.2 Ma, respectively. The No. 15 Fault System played a critical role during hydrocarbon migration within the HDR in the third member of the Maokou Formation. Our study finds a close link between the reactivation periods of this fault system and distinct hydrocarbon influxes in the study area.

5.3. Sources and genesis of natural gas

The formation temperatures of the third member of the Maokou Formation were below 100 °C and 120 °C during the first and second episodes of gas charging (Fig. 9), respectively. These temperatures were lower than the crude oil cracking temperature, indicating that the two episodes of natural gas in the HDR were not a result of crude oil cracking. The Qiongzhusi Formation source rock comprises black shale and mudstone, which are sapropelic (II) with TOC content ranging from 0.09 wt% to 6.12 wt% (1.94 wt% on average) (Zou et al., 2014). In the study area, the thickness of the Qiongzhusi Formation source rock ranges from 100 m to 150 m

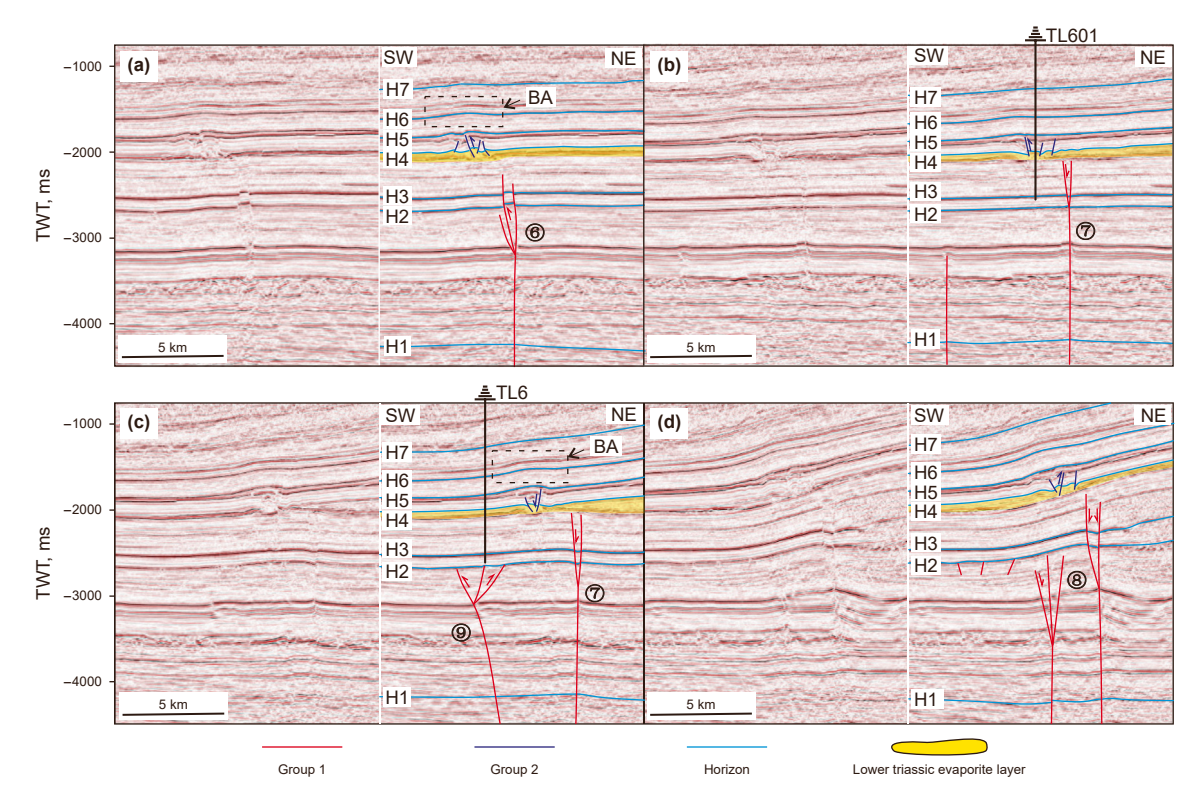


Fig. 12. Seismic profiles across No. 15 Fault System depicting the geometry of strike faults in the study area. **(a)**: Seismic profiles across fault segment 6. **(b)**: Seismic profiles across fault segment 7. **(c)**: Seismic profiles across fault segments 8. The 2 groups of the faults identified near the Tailai Gas Field comprise: (1) Group 1 was mainly offset the base of Middle Triassic Leikoupo Formation (Horizon H4); (2) Group 2 was mainly bounded by the base of Middle Triassic Leikoupo Formation (Horizon H4) and Upper Triassic Xujiahe Formation (Horizon H5).

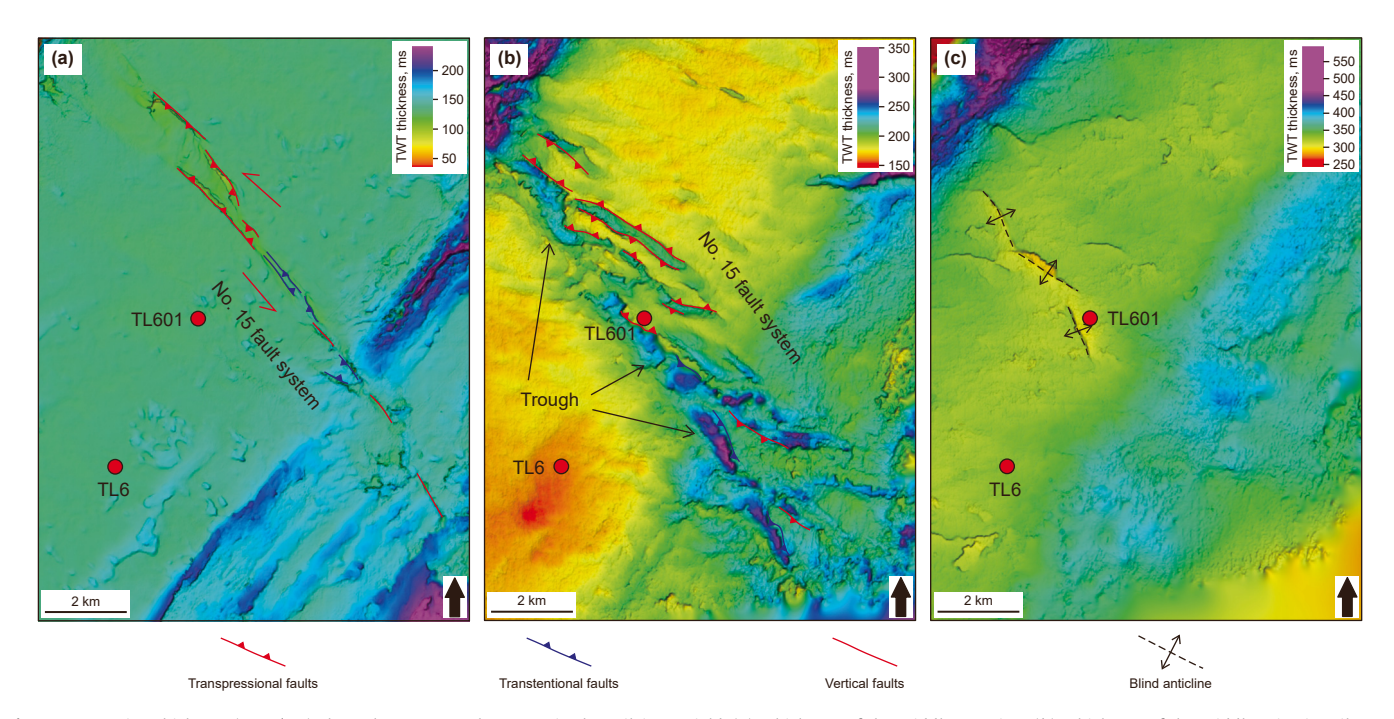


Fig. 13. Formation thickness (TWT/ms) along the No. 15 Fault System in the Tailai Gas Field. (a): Thickness of the Middle Permian; (b): Thickness of the Middle Triassic Leikoupo Formation; (c): Thickness of the 2nd member of Ziliujing Formation to Xiashaximiao Formation. Blue dotted rectangle in Fig. 11 shows the location of Fig. 13.

(Fig. 14(a); Qiu et al., 2021). The Wufeng-Longmaxi Formation source rock, composed mainly of black shale and dark gray mudstone, is predominantly sapropelic (II), with TOC exceeding 2.0 wt% (Li et al., 2021). This source rock was primarily developed in

the eastern and southern Sichuan Basin, with a thickness ranging from 40 to 80 m in the study area (Fig. 14(b)). The source rock in the first member of the Maokou Formation primarily comprises dark gray marl, which is categorized as humic-sapropelic (II) with TOC

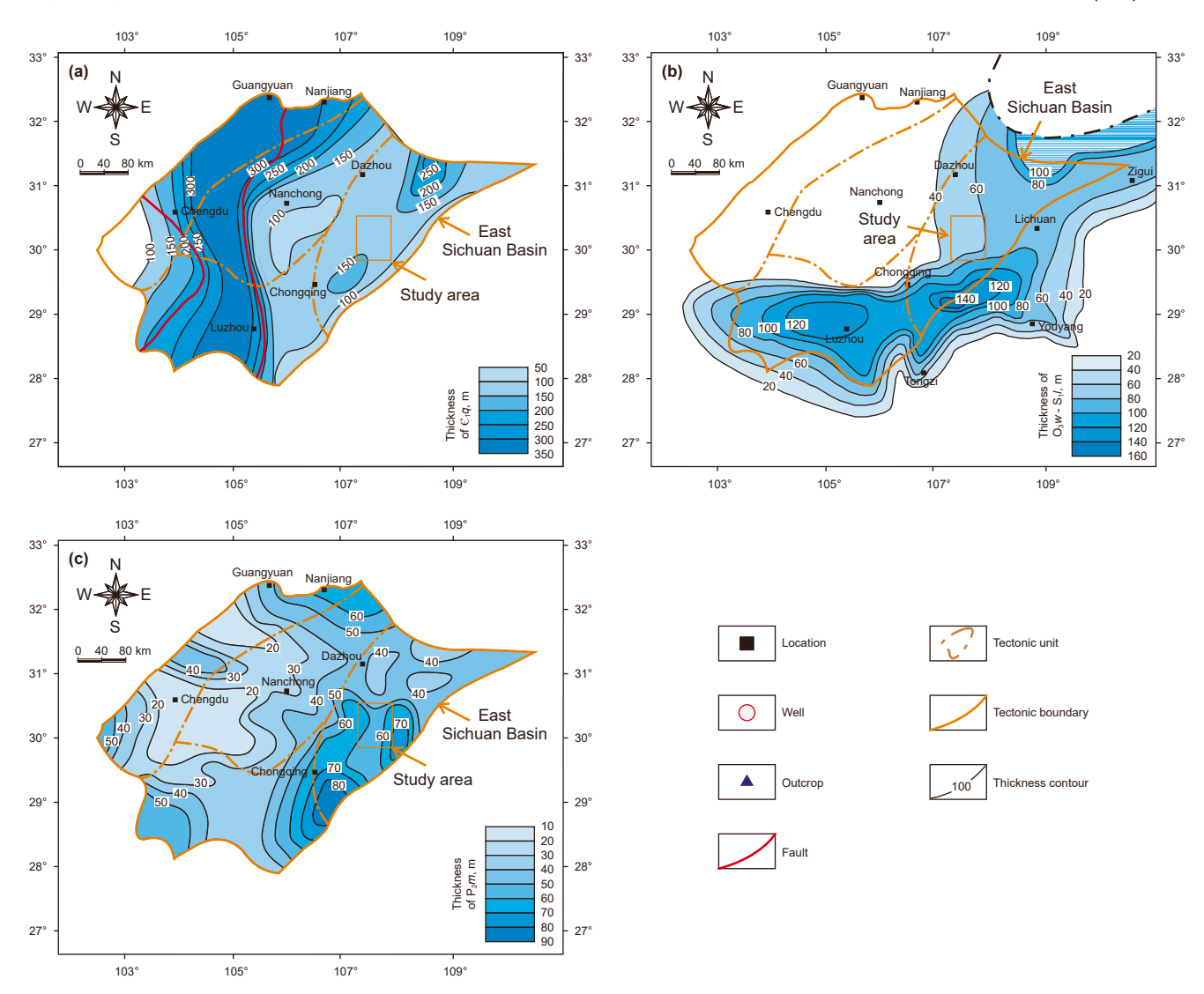


Fig. 14. The thickness distribution of source rocks in the Qiongzhusi Formation ((a), modified after Qiu et al., 2021), Wufeng—Longmaxi Formation ((b), modified after Sun et al., 2021) and the first member of the Maokou Formation ((c), modified from Li, 2021) in the Sichuan Basin.

ranging from 0.75 wt% to 1.50 wt% (Li et al., 2021). In the Tailai Gas Field, the thickness of the source rock in the first member of the Maokou Formation ranges from 40 to 70 m (Fig. 14(c)). The source rocks in the Qiongzhusi Formation, Wufeng-Longmaxi Formation and the first member of the Maokou Formation are all likely contributors of hydrocarbons to the HDR in the third member of the Maokou Formation.

The Emei magmatism in the Late Permian and rapid subsidence during the Early and Middle Triassic accelerated the maturity of the source rocks in the Qiongzhusi Formation, Wufeng-Longmaxi Formation and the first member of the Maokou Formation (Figs. 9 and 10; Shellnutt, 2014). During the episode of oil charging at around 246.9 Ma, the maturity of the source rocks in the Qiongzhusi Formation, Wufeng-Longmaxi Formation and the first member of the Maokou Formation were approximately 2.0%, 1.0% and 0.6%, respectively (Fig. 10). At the same time, the Qiongzhusi Formation source rock reached the stage of dry gas generation. The Wufeng-Longmaxi source rock was in the stage of significant oil generation, and the source rock in the first member of the Maokou Formation had just entered the threshold of oil generation. The maturity levels of source rocks in the Qiongzhusi Formation,

Wufeng-Longmaxi Formation and the first member of the Maokou Formation suggest that the oil predominantly originated from the Wufeng-Longmaxi Formation source rock (Fig. 15(a)), which is consistent with the conclusions in previous studies (Xie et al., 2020; Li et al., 2021).

During the first and second episodes of gas charging at approximately 222.4 Ma and 175.2 Ma respectively, simulations of the maturity history of source rocks indicate: 1) the Qiongzhusi Formation source rock had entered the stage of dry gas generation, with maturity of 2.0%-3.5%; 2) the Wufeng-Longmaxi Formation source rock had a maturity of 1.3%-2.0%, mainly in the stage of wet gas generation; 3) the maturity of the source rock in the first member of Maokou Formation ranged from 0.7% to 1.0%, mainly in the stage of oil generation (Fig. 10). The fault system provides the primary migration pathway for hydrocarbons in fault-related carbonate reservoirs (Wang et al., 2021). The timing of the first and second episodes of gas charging was synchronous with the activity of the No. 15 Fault System during the late stage of the Indosinian orogeny and the early stage of the Yanshanian orogeny, respectively (Fig. 15(b) and (c)). The No. 15 Fault System significantly eased gas migration during its reactivation periods (Fig. 15(b) and (c)).

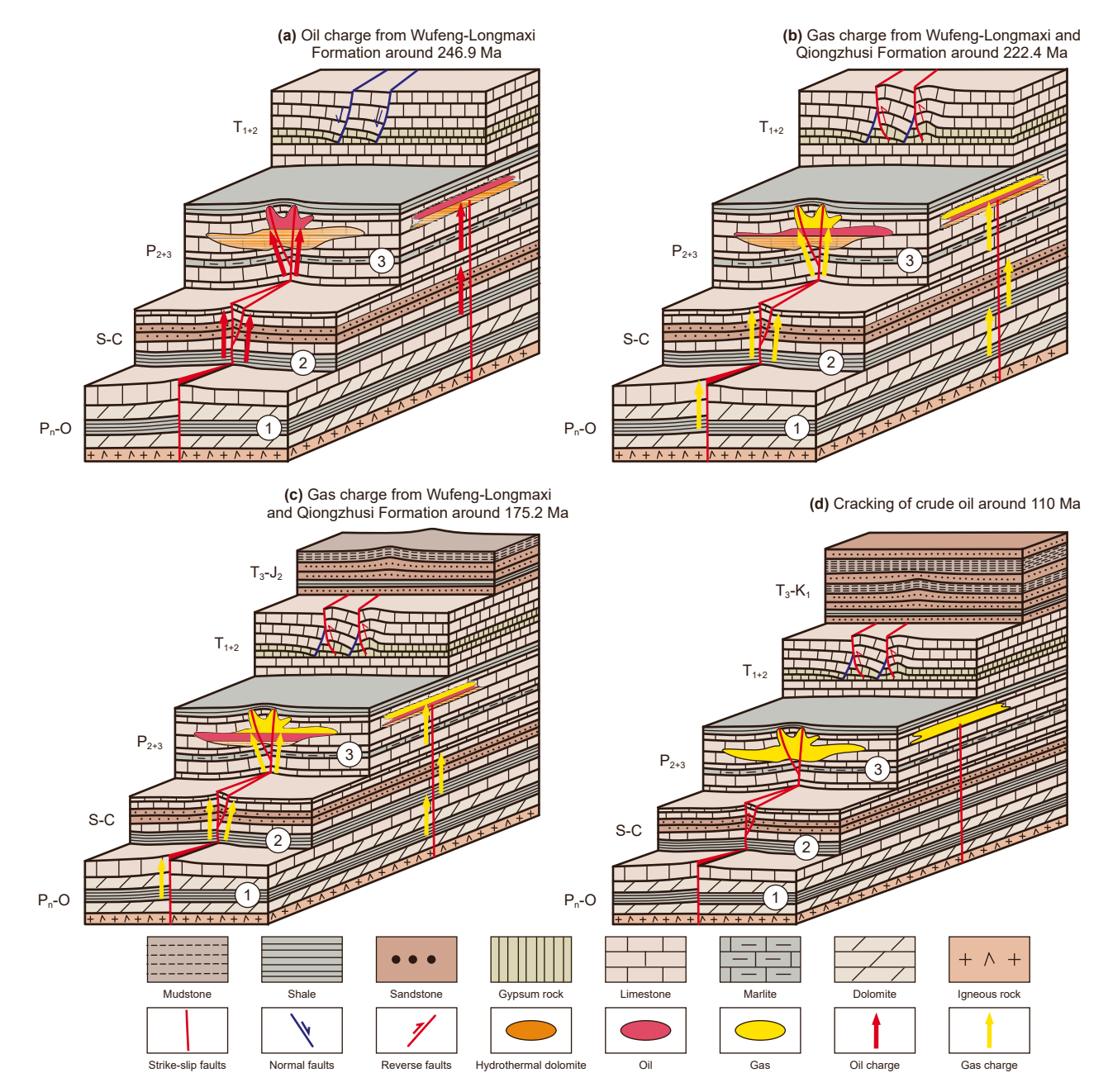


Fig. 15. The 3D schematic model showing the source of oil during the oil charging episode (a), the source of natural gas during the first (b) and second (c) episodes of gas charge, and the cracking of crude oil around 110 Ma (d). ①: Qiongzhusi Formation source rock; ②: Wufeng-Longmaxi Formation source rocks; ③: source rock in the first member of Middle Permian Maokou Formation.

Considering the timing of gas charging, the maturity of source rocks, and the reactivation periods of the No. 15 Fault System, the first and second episodes of natural gas likely had complex origins, including wet gas from the Wufeng-Longmaxi Formation source rock, as well as kerogen cracking gas or residual liquid hydrocarbon cracking gas in the Qiongzhusi Formation source rock (Fig. 15(b) and (c)). These results demonstrate that natural gas in deep and ultra-deep carbonate reservoirs partly originated directly from the source rocks in the ESB.

The HDR in the third member of the Maokou Formation reached its maximum burial depth, with a formation temperature of 220 °C at 110 Ma in the study area (Fig. 9), a value higher than the temperature necessary for the in-situ cracking of oil. The significant volumes of pyrobitumen trapped in Maokou Formation samples,

without liquid oil, appear to confirm that all crude oil has been cracked into gas around 110 Ma (Fig. 15(d)). The Tailai Gas Field is now primarily a gas reservoir with the contribution of in-situ oil cracking gas, wet gas from the Wufeng-Longmaxi Formation source rock, and kerogen cracking gas or residual liquid hydrocarbon cracking gas in the Qiongzhusi Formation source rocks.

6. Conclusions

Based on the investigation of hydrocarbon inclusions, geochemical analysis and in situ U-Pb dating of the calcite cements, maturity modeling of source rocks, and the variation of the stratigraphic thickness along the No. 15 Fault System, the following conclusions can be drawn.

- Oil charging into the HDR of the Maokou Formation occurred at approximately 246.9 Ma, coinciding with reactivation of the No. 15 Fault System during the early stage of the Indosinian orogeny. The first and second episodes of gas charging occurred at approximately 222.4 Ma and 175.2 Ma, respectively, induced by activities of the No. 15 Fault System during the late stage of the Indosinian orogeny and the early stage of the Yanshanian orogeny.
- 2. The hydrocarbon generation and charging history suggests that: 1) the paleo-oil pools within the HDR of the Maokou Formation was sourced from the Wufeng-Longmaxi Formation at approximately 246.9 Ma. 2) the first and second episodes of gas charge likely comprised wet gas from the Wufeng-Longmaxi Formation, and kerogen cracking gas or residual liquid hydrocarbon cracking gas from the Qiongzhusi Formation. Subsequently, the paleo-oil pools in the HDR underwent thermal cracking to natural gas at approximately 110 Ma, when the Maokou Formation reached temperatures of 220 °C.
- 3. The Tailai Gas Field has the contribution of in-situ oil cracking gas, wet gas, and kerogen cracking gas or residual liquid hydrocarbon cracking gas. The origins of natural gas in the deep and ultra-deep carbonate reservoirs were not solely crude oil cracking gas in the Sichuan Basin. Instead, they contain contributions from wet gas, kerogen cracking gas, or residual liquid hydrocarbon cracking gas directly from source rocks.

CRediT authorship contribution statement

Yan-Xian Zhu: Writing — original draft, Methodology, Conceptualization. Zhi-Liang He: Funding acquisition, Supervision, Writing — review & editing. Xiao-Wen Guo: Writing — review & editing, Supervision, Funding acquisition. Long Li: Writing — review & editing. Kamaldeen O.L. Omosanya: Writing — review & editing. Jian Gao: Resources. Ze Tao: Resources. Xue-Song Lu: Supervision.

Declaration of competing interest

The authors declare that they have no known competing financial interests or personal relationships that could have appeared to influence the work reported in this paper.

Acknowledgments

This study was financially supported by National Natural Science Foundation of China (No. 92255302) and the Joint Funds of the National Natural Science Foundation of China (No. U20B6001). We thank Petroleum Science Editor Dr. Hao Jie and reviewers for the constructive suggestions. We thank Xue-Song Lu for help with insitu U-Pb dating. The Petroleum Exploration and Production Research Institute of SINOPEC is thanked for providing background geological data.

Appendix A. Supplementary data

Supplementary data to this article can be found online at https://doi.org/10.1016/j.petsci.2025.02.004.

References

- Abanda, P.A., Hannigan, R.E., 2006. Effect of diagenesis on trace element partitioning in shales. Chem. Geol. 230 (1), 42–59. https://doi.org/10.1016/j.chemgeo.2005.11.011.
- Bhattacharya, S., Sharma, S., Agrawal, V., Dix, M.C., Zanoni, G., Birdwell, J.E., Wylie, A.S., Wagner, T., 2024. Influence of organic matter thermal maturity on

rare earth element distribution: a study of middle devonian black shales from the appalachian basin, USA. Energies 17 (9), 2107. https://doi.org/10.3390/en17092107

- Burke, E.A.J., 2001. Raman microspectrometry of fluid inclusions. Lithos 55 (1), 139–158. https://doi.org/10.1016/S0024-4937(00)00043-8.
- Cai, C., Xiang, L., Yuan, Y., Xu, C., He, W., Tang, Y., Borjigin, T., 2017. Sulfur and carbon isotopic compositions of the Permian to Triassic TSR and non-TSR altered solid bitumen and its parent source rock in NE Sichuan Basin. Org. Geochem. 105, 1—12. https://doi.org/10.1016/j.orggeochem.2016.12.004.
- Cazzini, F., Zotto, O.D., Fantoni, R., Ghielmi, M., Ronchi, P., Scotti, P., 2015. Oil and gas in the adriatic foreland, Italy. J. Petrol. Geol. 38 (3), 255–279. https://doi.org/ 10.1111/jpg.12610.
- Charvet, J., 2013. The neoproterozoic—early paleozoic tectonic evolution of the South China block: an overview. J. Asian Earth Sci. 74, 198—209. https://doi.org/10.1016/j.jseaes.2013.02.015.
- Chen, J.X., Guo, X.W., Tao, Z., Cao, Z.C., Wang, B., Zhang, X.Y., Xu, H., Zhao, J.X., 2022. U-Pb dating of oil charge in superimposed basins: a case study from the Tarim Basin, NW China. GSA Bull 134 (11–12), 3176–3188. https://doi.org/10.1130/B36324.1.
- Chen, Z., Simoneit, B.R.T., Wang, T.G., Ni, Z., Yuan, G., Chang, X., 2018. Molecular markers, carbon isotopes, and rare earth elements of highly mature reservoir pyrobitumens from Sichuan Basin, southwestern China: implications for PreCambrian-Lower Cambrian petroleum systems. Precambr. Res. 317, 33—56. https://doi.org/10.1016/j.precamres.2018.08.005.
- Chi, G., Diamond, L.W., Lu, H., Lai, J., Chu, H., 2021. Common problems and pitfalls in fluid inclusion study: a review and discussion. Minerals 11 (1), 7. https:// doi.org/10.3390/min11010007.
- Cong, F., Tian, J., Hao, F., Licht, A., Liu, Y., Cao, Z., Eiler, J.M., 2021. A thermal pulse induced by a permian mantle plume in the Tarim basin, northwest China: constraints from clumped isotope thermometry and in situ calcite U-Pb dating. J. Geophys. Res. Solid Earth 126 (4). https://doi.org/10.1029/2020JB020636.
- Deng, B., Liu, S.G., Liu, S., Li, Z.W., Zhao, J.C., 2009. Restoration of exhumation thickness and its significance in Sichuan Basin, China. J. Chengdu Univ. Technol. (Sci. Technol. Ed.) 36 (6), 675–686. https://doi.org/10.3969/j.issn.1671-9727.2009.06.013.
- Faramawy, S., Zaki, T., Sakr, A.A.E., 2016. Natural gas origin, composition, and processing: a review. J. Nat. Gas Sci. Eng. 34, 34–54. https://doi.org/10.1016/j.jngse.2016.06.030.
- Goldstein, R.H., 2001. Fluid inclusions in sedimentary and diagenetic systems. Lithos 55 (1–4), 159–193. https://doi.org/10.1016/S0024-4937(00)00044-X.
- Gu, Z., Wang, Z., 2014. The discovery of neoproterozoic extensional structures and its significance for gas exploration in the central sichuan block, Sichuan Basin, South China. Sci. China Earth Sci. 57, 2758–2768. https://doi.org/10.1007/ s11430-014-4961-x.
- Gu, Z.D., Wang, X., Nunns, A., Zhang, B., Jiang, H., Fu, L., Zhai, X.F., 2021. Structural styles and evolution of a thin-skinned fold-and-thrust belt with multiple detachments in the eastern Sichuan Basin, South China. J. Struct. Geol. 142, 104191. https://doi.org/10.1016/j.jsg.2020.104191.
- Guo, X., Hu, D., Huang, R., Wei, Z., Duan, J., Wei, X., Fan, X., Miao, Z., 2020. Deep and ultra-deep natural gas exploration in the Sichuan Basin: progress and prospect. Nat. Gas. Ind. B. 7 (5), 419–432. https://doi.org/10.1016/j.ngib.2020.05.001.
- Harrowfield, M.J., Wilson, C.J., 2005. Indosinian deformation of the Songpan Garze fold belt, northeast Tibetan Plateau. J. Struct. Geol. 27 (1), 101–117. https:// doi.org/10.1016/j.jsg.2004.06.010.
- He, D., Jia, C., Zhao, W., Xu, F., Luo, X., Liu, W., Tang, Y., Gao, S., Zheng, X., Li, D., Zhang, N., 2023. Research progress and key issues of ultra-deep oil and gas exploration in China. Petrol. Explor. Dev. 50 (6), 1333–1344. https://doi.org/10.1016/S1876-3804(24)60470-2.
- He, D.F., Li, D.S., Zhang, G.W., Zhao, L.Z., Fan, C., Lu, R.Q., Wen, Z., 2011. Formation and evolution of multi-cycle superposed Sichuan Basin, China. Chin. J. Geol. 46 (3), 589–606. https://doi.org/10.3969/j.issn.0563-5020.2011.03.001.
- He, S., Middleton, M., 2002. Heat flow and thermal maturity modelling in the northern carnarvon basin, north west shelf, Australia. Mar. Petrol. Geol. 19 (9), 1073–1088. https://doi.org/10.1016/S0264-8172(03)00003-5.
- He, Z., Li, S., Li, Y., Gao, J., 2022. Multi-directional and multiphase tectonic modification, and hydrocarbon differential enrichment in the middle-upper Yangtze region. J. Earth Sci. 33 (5), 1246–1259. https://doi.org/10.1007/s12583-022-1738-6.
- Huang, D., 2019. Jurassic integrative stratigraphy and timescale of China. Sci. China Earth Sci. 62, 223–255. https://doi.org/10.1007/s11430-017-9268-7.
- Huang, S., Jiang, Q., Jiang, H., Tang, Q., Zeng, F., Lu, W., Hao, C., Yuan, M., Wu, Y., 2023. Genetic and source differences of gases in the middle permian qixia and Maokou formations in the Sichuan Basin, SW China. Org. Geochem. 178, 104574. https://doi.org/10.1016/j.orggeochem.2023.104574.
- Huang, S.P., Fang, X., Liu, D., Fang, C.C., Huang, T.F., 2015. Natural gas genesis and sources in the zizhou gas field, ordos basin, China. Int. J. Coal Geol. 152, 132–143. https://doi.org/10.1016/j.coal.2015.10.005.
- Jiang, Q., Qiu, N.S., Zhu, C.Q., 2018. Heat flow study of the emeishan large igneous province region: implications for the geodynamics of the emeishan mantle plume. Tectonophysics 724–725, 11–27. https://doi.org/10.1016/ j.tecto.2017.12.027.
- Jin, X.D., Pan, C.C., Yu, S., Li, E.T., Wang, J., Fu, X.D., Qin, J.Z., Xie, Z.Y., Zheng, P., Wang, L.S., Chen, J.P., Tan, Y.M., 2014. Organic geochemistry of marine source rocks and pyrobitumen-containing reservoir rocks of the Sichuan Basin and neighbouring areas, SW China. Mar. Petrol. Geol. 56, 147–165. https://doi.org/

10.1016/j.marpetgeo.2014.04.010.

- Kendrick, M.A., Zhao, J., Feng, Y., 2022. Early accretion and prolonged carbonation of the Pacific Ocean's oldest crust. Geology 50 (11), 1270—1275. https://doi.org/ 10.1130/G49985.1.
- Kotarba, M.J., Więcław, D., Jurek, K., Waliczek, M., 2022. Variations of bitumen fraction, biomarker, stable carbon isotope and maceral compositions of dispersed organic matter in the Miocene strata (Carpathian Foredeep, Poland) during maturation simulated by hydrous pyrolysis. Mar. Petrol. Geol. 137, 105487. https://doi.org/10.1016/j.marpetgeo.2021.105487.
- Li, C.X., He, D.F., Sun, Y.P., He, J.Y., Jiang, Z.X., 2015a. Structural characteristic and origin of intra-continental fold belt in the eastern Sichuan basin, South China Block. J. Asian Earth Sci. 111, 206–221. https://doi.org/10.1016/j.iseaes.2015.07.027.
- Li, L., Bao, Z., Li, L., Li, Z., Ban, S., Li, Z., Wang, T., Li, Y., Zheng, N., Zhao, C., Chen, L., 2024. The source and preservation of lacustrine shale organic matter: insights from the qingshankou Formation in the changling sag, southern songliao basin, China. Sediment. Geol. 466, 106649. https://doi.org/10.1016/j.sedgeo.2024.106649.
- Li, Q.Q., Li, B., Mei, W.H., Liu, Y.L., 2022. Genesis and sources of natural gas in foldand-thrust belt: the middle permian in the NW Sichuan Basin. Mar. Petrol. Geol. 140, 105638. https://doi.org/10.1016/j.marpetgeo.2022.105638.
- Li, S., 2021. The distribution of source rocks and hydrocarbon accumulation model of the permian Maokou Formation in Sichuan Basin, master's thesis. China Univ. Pet. Beijing 38. https://doi.org/10.27643/d.cnki.gsybu.2021.000233.
- Li, S.Z., Santosh, M., Zhao, G.C., Zhang, G.W., Jin, C., 2012. Intracontinental deformation in a frontier of super-convergence: a perspective on the tectonic milieu of the South China Block. J. Asian Earth Sci. 49, 313–329. https://doi.org/10.1016/j.jseaes.2011.07.026.
- Li, W., Liu, J.J., Deng, S.H., Zhang, B.M., Zhou, H., 2015b. The nature and role of Late Sinian-Early Cambrian tectonic movement in Sichuan Basin and its adjacent areas. Acta Pet. Sin. 36 (5), 546–556. https://doi.org/10.7623/syxb201505003.
- Li, Y., Ding, W., Zeng, T., Xia, W., Cheng, X., Shi, S., Ding, S., 2023. Structural geometry and kinematics of a strike-slip fault zone in an intracontinental thrust system: a case study of the No. 15 fault zone in the Fuling area, eastern Sichuan Basin, southwest China. J. Asian Earth Sci. 242, 105512. https://doi.org/10.1016/i.jseaes.2022.105512.
- Li, Y., Gao, J., Han, J., Yang, Y.E., 2019. Geophysical evidence for thrusting of crustal materials from orogenic belts over both sides of the Yangtze Block and its geological significance. Sci. China Earth Sci. 62, 812–883. https://doi.org/ 10.1007/s11430-018-9290-0.
- Li, Y.J., Xu, F.B., Zeng, L.Y., Zhang, W.J., Li, M.L., Liao, Y.S., Chen, W.D., 2021. Gas source in lower permian Maokou Formation and gas accumulation in the syncline area of eastern Sichuan Basin. J. Pet. Sci. Eng. 206, 109044. https://doi.org/10.1016/j.petrol.2021.109044.
- Liang, T., Zhan, Z.W., Gao, Y., Wang, Y.P., Zou, Y.R., Peng, P., 2020. Molecular structure and origin of solid bitumen from northern Sichuan Basin. Mar. Petrol. Geol. 122, 104654. https://doi.org/10.1016/j.marpetgeo.2020.104654.
- Liang, X.Q., Zhou, Y., Jiang, Y., Wen, S.N., Fu, J.G., Wang, C., 2013. Difference of sedimentary response to Dongwu movement: study on LA-ICPMS U-Pb ages of detrital zircons from upper permian wujiaping or Longtan Formation from the Yangtze and cathaysia blocks. Acta Petrol. Sin. 29 (10), 3592–3606 (in Chinese).
- Liu, H., Wang, Y., Li, Z., Zi, J.W., Huangfu, P., 2018a. Geodynamics of the indosinian orogeny between the South China and Indochina blocks: insights from latest permian—triassic granitoids and numerical modeling. GSA Bull 130 (7–8), 1289–1306. https://doi.org/10.1130/B31904.1.
- Liu, Q., Wu, X., Wang, X., Jin, Z., Zhu, D., Meng, Q., Huang, S., Liu, J., Fu, Q., 2019. Carbon and hydrogen isotopes of methane, ethane, and propane: a review of genetic identification of natural gas. Earth Sci. Rev. 190, 247–272. https:// doi.org/10.1016/j.earscirev.2018.11.017.
- Liu, S., Deng, B., Jansa, L., Li, Z., Sun, W., Wang, G., Luo, Z., Yong, Z., 2018b. Multi-stage basin development and hydrocarbon accumulations: a review of the Sichuan Basin at eastern margin of the Tibetan plateau. J. Earth Sci. 29, 307–325. https:// doi.org/10.1007/s12583-017-0904-8.
- Liu, S.G., Yang, Y., Deng, B., Zhong, Y., Wen, L., Sun, W., Li, Z.W., Jansa, L., Li, J.X., Song, J.M., Zhang, X.H., Peng, H.L., 2021. Tectonic evolution of the Sichuan Basin, southwest China. Earth Sci. Rev. 213, 103470. https://doi.org/10.1016/j.earscirev.2020.103470.
- Loucks, R.G., Dutton, S.P., 2019. Insights into deep, onshore Gulf of Mexico Wilcox sandstone pore networks and reservoir quality through the integration of petrographic, porosity and permeability, and mercury injection capillary pressure analyses. AAPG Bull. 103 (3), 745–765. https://doi.org/10.1306/09181817366.
- Ludwig, K., 2012. Isoplot/Ex, v. 3.75, A Geochronological Toolkit for Microsoft Excel. Berkeley Geochronol. Cent. Spec. Publ. 5, p. 75.
- McLennan, S.M., 1989. Rare earth elements in sedimentary rocks: influence of provenance and sedimentary processes. Geochem. Mineral. Rare Earth Elem. 169–200. https://doi.org/10.1515/9781501509032-010.
- Millson, J.A., Quin, J.G., Idiz, E., Turner, P., Al-Harthy, A., 2008. The Khazzan gas accumulation, a giant combination trap in the Cambrian Barik Sandstone Member, Sultanate of Oman: implications for Cambrian petroleum systems and reservoirs. AAPG Bull. 92 (7), 885–917. https://doi.org/10.1306/02210807100.
- Ni, Z., Zhao, J.X., Feng, Y., Liu, H., Liu, F., Zhou, W., Luo, B., 2024a. Geochemical, isotopic, and U-Pb geochronological constraints on multiple dolomitization and petroleum charging events in Precambrian carbonate reservoirs in the Sichuan Basin, China. Mar. Petrol. Geol. 165, 106908. https://doi.org/10.1016/

j.marpetgeo.2024.106908.

- Ni, Z., Zhao, J.X., Feng, Y., Zhou, W., Yang, C., Liu, H., Shao, G., Luo, B., 2024b. Age and origin of Sinian grape-lace shaped dolostone in central Sichuan Basin. Acta Petrol. Sin 40 (1), 282–294. https://doi.org/10.18654/1000-0569/2024.01.15.
- Omosanya, Johansen, S.E., Harishidayat, D., 2015. Evolution and character of suprasalt faults in the easternmost hammerfest basin, SW barents sea. Mar. Petrol. Geol. 66, 1013–1028. https://doi.org/10.1016/j.marpetgeo.2015.08.010.
- Omosanya, K.O., 2018. Episodic fluid flow as a trigger for Miocene-Pliocene slope instability on the Utgard High, Norwegian Sea. Basin Res. 30, 942–964. https://doi.org/10.1111/bre.12288.
- Omosanya, K.O., 2020. Cenozoic tectonic inversion in the naglfar dome, Norwegian north sea. Mar. Petrol. Geol. 118, 104461. https://doi.org/10.1016/j.marpetgeo.2020.104461.
- Pan, L., Hu, A., Liang, F., Jiang, L., Hao, Y., Feng, Y., Shen, A., Zhao, J., 2021. Diagenetic conditions and geodynamic setting of the middle Permian hydrothermal dolomites from southwest Sichuan Basin, SW China: insights from in situ U–Pb carbonate geochronology and isotope geochemistry. Mar. Petrol. Geol. 129, 105080. https://doi.org/10.1016/j.marpetgeo.2021.105080.
- Pan, L., Xu, Z.X., Li, R.B., Zou, Y.T., 2020. Basement Fault characterization and hydrocarbon accumulation in fuling of southeastern Sichuan. Spec. Oil Gas Reserv. 27 (4), 19–25. https://doi.org/10.3969/j.issn.1006-6535.2020.04.003.
- Paton, C., Hellstrom, J., Paul, B., Woodhead, J., Hergt, J., 2011. Iolite: freeware for the visualisation and processing of mass spectrometric data. J. Anal. At. Spectrom. 26 (12), 2508–2518. https://doi.org/10.1039/c1ja10172b.
- Peng, J., Hu, Z., Feng, D., Wang, Q., 2022. Sedimentology and sequence stratigraphy of lacustrine deep-water fine-grained sedimentary rocks: the lower jurassic dongyuemiao Formation in the Sichuan Basin, western China. Mar. Petrol. Geol. 146, 105933. https://doi.org/10.1016/j.marpetgeo.2022.105933.
- Peters, K.E., Walters, C.C., Moldowan, J.M., 2005. The biomarker guide. Biomarkers and Isotopes in the Petroleum Exploration and Earth History, Second Ed, vol. 2. Cambridge Univ. Press. Cambridge, pp. 475—1155.
- Cambridge Univ. Press, Cambridge, pp. 475—1155.

 Qiu, N., Liu, W., Fu, X., Li, W., Xu, Q., Zhu, C., 2021. Maturity evolution of lower cambrian Qiongzhusi Formation shale of the Sichuan Basin. Mar. Petrol. Geol. 128, 105061. https://doi.org/10.1016/j.marpetgeo.2021.105061.
- Qiu, N.S., Chang, J., Zhu, C.Q., Liu, W., Zuo, Y.H., Xu, W., Li, D., 2022. Thermal regime of sedimentary basins in the Tarim, upper Yangtze and north China cratons, China. Earth Sci. Rev. 224, 103884. https://doi.org/10.1016/j.earscirev.2021.103884.
- Robbins, L.J., et al., 2016. Trace elements at the intersection of marine biological and geochemical evolution. Earth Sci. Rev. 163, 323–348. https://doi.org/10.1016/i.earscirey.2016.10.013.
- Roberts, N.M.W., Drost, K., Horstwood, M.S.A., Condon, D.J., Chew, D., Drake, H., Milodowski, A.E., McLean, N.M., Smye, A.J., Walker, R.J., Haslam, R., Hodson, K., Imber, J., Beaudoin, N., Lee, J.K., 2020. Laser ablation inductively coupled plasma mass spectrometry (LA-ICP-MS) U-Pb carbonate geochronology: strategies, progress, and limitations. Geochronology 2 (1), 33—61. https://doi.org/10.5194/gchron-2-33-2020.
- Roberts, N.M.W., Žák, J., Vacek, F., Sláma, J., 2021. No more blind dates with calcite: fluid-flow vs. fault-slip along the Očkov thrust, Prague Basin. Geosci. Front. 12 (4), 101143. https://doi.org/10.1016/j.gsf.2021.101143.
- Shellnutt, J.G., 2014. The Emeishan large igneous province: a synthesis. Geosci. Front. 5 (3), 369–394. https://doi.org/10.1016/j.gsf.2013.07.003.
- Shi, H., Shi, X., Glasmacher, U.A., Yang, X., Stockli, D.F., 2016. The evolution of eastern Sichuan Basin, Yangtze block since Cretaceous: constraints from low temperature thermochronology. J. Asian Earth Sci. 116, 208–221. https://doi.org/10.1016/ j.jseaes.2015.11.008.
- Shiroodi, S.K., Ghafoori, M., Faghih, A., Ghanadian, M., Lashkaripour, G., Moghadas, N.H., 2015. Multi-phase inversion tectonics related to the hendijan-nowrooz-khafji fault activity, zagros mountains, SW Iran. J. Afr. Earth Sci. 111, 399–408. https://doi.org/10.1016/j.jafrearsci.2015.08.015.
- Su, G.P., Li, Z.Q., Ying, D.L., Li, G., Ying, W.F., Yang, Y.Y., Liu, H.L., Ding, X., Tang, H.Q., 2020. Formation and evolution of the Caledonian paleo-uplift and its genetic mechanism in the Sichuan Basin. Acta Geol. Sin. 94 (6), 1793–1812. https:// doi.org/10.19762/j.cnki.dizhixuebao.2020080.
- Sun, Z., Sun, W., Lin, J., Ma, Q., 2021. Hydrocarbon accumulation conditions and main controlling factors of the middle-upper cambrian xixiangchi group in the eastern Sichuan Basin. Pet. Geol. Exp. 43 (6), 933—940. https://doi.org/10.11781/ sysydz202106933.
- Tong, J., Chu, D., Liang, L., Shu, W., Song, H., Song, T., Song, H., Wu, Y., 2019. Triassic integrative stratigraphy and timescale of China. Sci. China Earth Sci. 62 (1), 189–222. https://doi.org/10.1007/s11430-018-9278-0.
- Volkman, J.K., Barrett, S.M., Dunstan, G.A., Jeffrey, S.W., 1994. Sterol biomarkers for microalgae from the green algal class Prasinophyceae. Org. Geochem. 21 (12), 1211–1218. https://doi.org/10.1016/0146-6380(94)90164-3.
- Wang, W., Pang, X., Chen, Z., Chen, D., Wang, Y., Yang, X., Luo, B., Zhang, W., Zhang, X., Li, C., Wang, Q., 2021. Quantitative evaluation of transport efficiency of fault-reservoir composite migration pathway systems in carbonate petroliferous basins. Energy 222, 119983. https://doi.org/10.1016/j.energy.2021.119983.
- Wang, W., Pang, X., Wang, Y., Chen, Z., Li, C., Ma, X., 2022. Hydrocarbon expulsion model and resource potential evaluation of high-maturity marine source rocks in deep basins: example from the Ediacaran microbial dolomite in the Sichuan Basin, China. Pet. Sci. 19 (6), 2618–2630. https://doi.org/10.1016/ j.petsci.2022.11.018.
- Xie, Z.Y., Yang, C.L., Dong, C.Y., Dai, X., Zhang, L., Guo, J.Y., Guo, Z.Q., Li, Z.S., Li, J.,

- Qi, X.N., 2020. Geochemical characteristics and genesis of middle devonian and middle permian natural gas in Sichuan Basin. China. J. Nat. Gas Geosci. 31 (4), 447–461. https://doi.org/10.11764/j.issn.1672-1926.2020.01.005.
- Yang, T., Azmy, K., He, Z., Li, S., Liu, E., Wu, S., Wang, J., Li, T., Gao, J., 2022. Fault-controlled hydrothermal dolomitization of Middle Permian in southeastern Sichuan Basin, SW China, and its temporal relationship with the Emeishan Large Igneous Province: new insights from multi-geochemical proxies and carbonate U—Pb dating. Sediment. Geol. 439, 106215. https://doi.org/10.1016/j.sedgeo.2022.106215.
- Zhang, G.W., Guo, A.L., Wang, Y.J., Li, S.Z., Dong, Y.P., Liu, S.F., He, D.F., Cheng, S.Y., Lu, R.K., Yao, A.P., 2013. Tectonics of South China continent and its implications. Sci. China Earth Sci. 56 (11), 1804–1828. https://doi.org/10.1007/s11430-013-4679-1.
- Zhang, J.L., Qiao, S.H., Lu, W.J., Hu, Q.C., Chen, S.G., Liu, Y., 2016. An equation for determining methane densities in fluid inclusions with Raman shifts. J. Geochem. Explor. 171, 20–28. https://doi.org/10.1016/j.gexplo.2015.12.003.
- Zhang, T., Lin, J.H., Han, Y.Q., Wang, Z.Y., Qin, J., Zhang, R.Q., 2020. Pattern of hydrothermal dolomitization in the middle permian Maokou Formation, eastern Sichuan Basin, and its alteration on reservoirs herein. Oil Gas Geol. 41 (1), 132–143+200. https://doi.org/10.11743/ogg20200112.
- Zhang, X., Shen, B., Yang, J., Sun, W., Hou, D., 2021. Evolution characteristics of maturity-related sterane and terpane biomarker parameters during hydrothermal experiments in a semi-open system under geological constraint. J. Pet. Sci. Eng. 201, 108412. https://doi.org/10.1016/j.petrol.2021.108412.
- Zheng, C., Xu, C., Brix, M.R., Zhou, Z., 2019. Evolution and provenance of the Xuefeng intracontinental tectonic system in South China: constraints from detrital zircon fission track thermochronology. J. Asian Earth Sci. 176, 264–273. https://doi.org/10.1016/j.jseaes.2019.02.012.
- Zou, C.N., Wei, G.Q., Xu, C.C., Du, J.H., Xie, Z.Y., Wang, Z.C., Hou, L.H., Yang, C., Li, J., Yang, W., 2014. Geochemistry of the sinian—cambrian gas system in the Sichuan Basin, China. Org. Geochem. 74, 13–21. https://doi.org/10.1016/j.orggeochem.2014.03.004.